Modeling Earth Systems and Environment (2026) 12:77
https://doi.org/10.1007/s40808-025-02715-2

ORIGINAL ARTICLE

Sensitivity study of WRF model in capturing extreme rainfall associated to an MCS over Central India on 15–17 September 2023

Parvathy Thankachy P[1] · **Saurabh Das**[1]

Received: 18 July 2025 / Accepted: 27 December 2025

Abstract

Accurate representation of extreme rainfall events (EREs) associated with Mesoscale Convective Systems (MCSs) is a serious challenge for weather prediction models at convection-permitting resolutions. Central India, a part of the Monsoon Core Zone (MCZ), is one of the regions where MCS events are active, particularly during the Indian summer monsoon. Between 15 and 17 September 2023, multiple EREs and heavy rainfall events (HREs) occurred that caused the highest rainfall over Madhya Pradesh in the last few decades and led to floods and flood-like situations. To study this event, using various combinations of physical parameterization schemes, 18 simulations were carried out in a triple-nested domain, with the third domain having a resolution of 2 km over Madhya Pradesh. For this event, Set 8 (Thompson MP + KF CU+ YSU PBL) was found to exhibit the best performance. The model was found to capture the MCS features, although it was weaker than that in the Indian Monsoon Data Assimilation and Analysis (IMDAA) reanalysis dataset. The system is identified to primarily be low-to-mid level that extended up to $\approx$ 17.5 km during peak rainfall. It is also observed, in contrary to the common practice, the use of Cumulus Parameterization in the convection permitting resolution improve the result significantly. These findings underscore the importance of scheme selection in simulating MCSs over Central India and contribute to improving forecast skills for high-impact weather events in the MCZ.

Keywords Sensitivity study · WRF · Mesoscale Convective System · Cloud microphysics · Convection · Extreme rainfall

Introduction

Over the past 50 years, the occurrence of extreme weather events (EWEs), such as extreme rainfall events (EREs) and tropical cyclones, has increased in number significantly (Rohini et al. 2016; Bjerge and Trifkovic 2018; Mohapatra and Sharma 2019), particularly over the Indian region. The increasing occurrence of EREs are majorly contributed by the warming of climate and anthropogenic activities (Ali and Mishra 2017; Singh and Goyal 2016; Boyaj et al. 2020; Aggarwal et al. 2022). EREs often lead to several other disasters, such as flash floods and landslides, causing severe damage to property and loss of lives. Therefore, a better understanding and accurate forecasting of these EREs is essential in order to take prior preventive measures.

The Weather Research and Forecasting (WRF) model has been used extensively to study various weather events such as EREs, heavy rainfall events (HREs), heatwaves, thunderstorms, and cyclones (Gupta et al. 2024; Mondal et al. 2024; Pérez-Alarcón et al. 2024; Ashok and Singh 2025). It features a wide variety of physics parameterization and dynamics schemes as discussed in Skamarock et al. (2021), enabling one for an optimal study at different scales, locations, and applications by choosing the best set of combinations. Although this offers a great window for flexibility, it also poses a challenge in choosing a suitable set of parameters for better prediction over a particular location.

Among the several physical parameterization schemes available in the WRF model, the microphysics (hereafter MP), cumulus (hereafter CU), planetary boundary layer (hereafter PBL), radiation, and land surface model (hereafter

✉ Saurabh Das
saurabh.das@iiti.ac.in; das.saurabh01@gmail.com

Parvathy Thankachy P
phd2301121011@iit.ac.in

[1] Department of Astronomy, Astrophysics and Space Engineering, Indian Institute of Technology Indore, Indore, India

LSM) schemes mainly influence the simulation of precipitation. The MP schemes simulate the water mass distribution among the different hydrometeors, such as cloud droplets, water vapor, rain, ice, and others. These schemes account for the formation and growth of clouds and precipitation processes and are always turned on in the model. They are scale-independent, whereas CU and PBL schemes are scale-dependent, and their performance will differ based on the resolution at which the model is run. CU schemes deal with the sub-grid scale processes associated with the convective clouds and play a role in removing the convective instability present in a grid cell. These schemes are designed with a trigger function that activates it under favorable conditions, thus influencing the evolution of convection. They are typically designed for the coarser resolutions, like 30 km. With an increase in computational resources, the models are now able to run even at 1 km. At resolutions finer than 10 km, known as the "Convective Grey Zone", the model is not capable of explicitly resolving the convection, and neither are the traditional CU schemes. The usage of CU scheme in this range is optional. However, for resolutions finer than 4 km, the model is considered to be capable of explicitly simulating convection, and it is generally suggested to turn off the CU scheme within this grid resolution to avoid double-counting of convection (Skamarock et al. 2021; Jee and Kim 2017; Liang et al. 2019).

However, several studies suggest that enabling CU even at these high resolutions can improve simulations, particularly for Mesoscale Convective System (hereafter MCS) events and HREs (Park et al. 2022; Deng and Stauffer 2006; Lee et al. 2011). In a study by Gimhan et al. (2023) the role of CU and MP schemes in simulating EREs were analyzed, the usage of Kain-Fritsch (KF) in the innermost domain of 3 km resolution was found to be more suitable in capturing the rainfall than when CU was turned off. Lee et al. (2011) studied multiple HREs over the Korean peninsula using a nested four domain configuration with the innermost domain at a resolution of 1 km. Sensitivity study was carried out by turning the CU scheme on and off up to the third domain of 3 km resolution. They found that usage of CU at a 3 km resolution improved the forecasts for those cases of weak synoptic forcings and large CAPE. For cases with strong synoptic forcing, CU schemes were found to suppress the MP schemes by making parts of the troposphere dry and warm. Tiwari and Bush (2025) found the usage of CU scheme even at a 3 km resolution is required to make an accurate prediction of precipitation. The study was on an extreme orographic rainfall over the Himalayas, which was driven by the strong monsoonal flow. Due to the complex topography, the model was unable to simulate explicit convection even at 3 km. KF acted as a catalyst in initiating the convection, which the grid-scale dynamics were sustaining further that led to the simulation of a realistic event. Seo and Ahn (2023) tried to see how the model is able to capture EREs during summer when CU is used at a 3 km resolution. Using CU was found to be useful for EREs of low intensity, but for short term high intense cases, simulation was better with CU turned off at this resolution. The usage of CU schemes within this "Convection-permitting resolution", therefore, remains an open research question.

Similarly, the model uses PBL parameterization schemes to account for the turbulent mixing associated with various processes, such as evaporation and heat transfer, that affect the PBL. Its structure and the processes that take place directly affect the weather and climate (Garratt 1994). As these processes have a scale of $\leq$ 1 km, the grey zone for these schemes are also at resolutions of the same range. The selection of the best combination of parameterization schemes is vital in simulating the events realistically, which ultimately helps in the understanding of atmospheric processes and associated dynamics (Mukherjee and Ramakrishnan 2022; Eiras-Barca et al. 2017; Milrad et al. 2017; Wang et al. 2022; Shaji et al. 2024). Jankov et al. (2005) studied multiple MCS events in the USA, and found that CU had the greatest impact on the simulations, followed by PBL and MP schemes. Evans et al. (2012) evaluated 4 rainfall events that belonged to four most common storm types over South-East Australia. However, no single combination was found to perform best across all the events consistently. Although they were unable to find a better performing MP scheme, they found that Mellor-Yamada-Janjic (MYJ) PBL and Betts-Miller-Janjic (BMJ) CU schemes can be used more preferably. In a sensitivity study conducted by Zhou et al. (2024) on summer precipitation over the Tibetan plateau, Thompson MP with Mellor-Yamada-Nakanishi-Niino (MYNN) 2.5 PBL and Tiedtke CU performed well in the grey zone region, along with those simulations with CU turned off. This study also highlighted the importance of PBL schemes and the impact it has on latent heat, which affects precipitation.

Over the Indian region, numerous such studies have been carried out to assess the impact of different MP or PBL schemes on various EREs (Gunwani and Mohan 2017; Gorja et al. 2023; Kadaverugu et al. 2021; Patil and Pradeep Kumar 2016). Although there have been studies on individual or paired scheme sensitivities, comprehensive evaluations of MP, PBL, and CU schemes together - especially for the simulation of EREs and HREs over India - are still relatively limited. Some studies carried out over the region of India are mentioned in Table 1.

Multiple studies have indicated that over the past few decades, there has been a decrease in the occurrence of moderate rainfall over Central India and a significant rise in the occurrence of EREs (Goswami et al. 2006; Pai and

Table 1 Summary of sensitivity studies evaluating different combinations of physical parameterization schemes over various regions in India

Study	Region and Resolution	Best Performing Combination	Remarks
Karrevula et al. (2024)	Bhubaneshwar; 0.5 km (innermost domain resolution)	Noah LSM + any MP + no CU; Thompson MP + Noah LSM + KF CU	32 simulations for capturing EREs
Srinivas et al. (2013)	India; 30 km resolution	BMJ CU	Studied over 10 summer monsoons over 7 rainfall zones
Chawla et al. (2018)	Upper Ganga Basin;3 km (innermost domain resolution)	Goddard MP + MYJ PBL + BMJ CU	Studying EREs
Sharma et al. (2024)	Mahi River Basin; 3 km (innermost domain resolution)	Goddard MP + KF CU + YSU/ ACM2 PBL	Studies HREs
Madhulatha and Rajeevan (2018)	Gadanki region; 2 km (innermost domain resolution)	Thompson MP + MYJ PBL + BMJ CU	Study focused on MCS simulation
Douluri and Chakraborty (2021)	West Coast; 9 km (innermost domain resolution)	Lin/Thompson MP + KF/GD CU	HREs associated with ARs

KF, BMJ, and GD CU are acronyms for Kain-Fritsch, Betts-Miller-Janjic, and Grell Devenyi CU schemes, respectively, and MYJ, YSU, and ACM2 correspond to Mellor-Yamada-Janjic, Yonsei University, and Asymmetric Convective Model v.2, respectively

Sridhar 2015). Being one of the major convection zones in India, this is also a region where MCS events are active. However, WRF sensitivity studies focusing on this region remain scarce. Therefore, high-resolution simulations over this region are essential to understand how the model performs with different physical parameterization schemes for a realistic representation of EREs. This can aid in improving forecasts, which can ultimately help in water management and disaster preparedness.

This study considers a case study of an ERE that occurred over the Central India region during 15-17 September 2023. This system, as it passed through the state of Madhya Pradesh, caused significant rainfall over regions like Bhimpur and Indore (IMD 2023f, g), with local news outlets reporting historical records being broken. IMD annual report mentioned this as one of those events for which rainfall amounts exceeded 1.5 times the daily long-term normal (i.e., daily long-period averaged) rainfall values over Central India between 15 and 17 September (IMD 2023a). 18 simulations are designed and carried out by varying 3 MP, 2 PBL, and 3 CU schemes at a convection-permitting resolution to see how the WRF model performs over this region in capturing this event. Best performing model is identified using a series of tests and a ranking system. The study also tries to analyze the factors that caused the event. The remainder of this paper is organized as follows: section Event description describes the event, followed by a model description in Section Model description. The datasets used and evaluation carried out are presented under Sections Datasets and Evaluation, respectively. Results and discussion are provided in Section Results, followed by summarizing the key conclusions drawn from the study in Section Discussions and conclusions.

Event description

Associated with a cyclonic circulation in the mid-tropospheric level over the east-central Bay of Bengal (BoB), which later moved towards the central part of BoB, a Low Pressure Area (LPA) was formed over the central and adjoining north part of BoB in the morning of 13 September 2023 (IMD 2023b, c, d, e). The LPA got more intensified and started to move in the west-northwestward direction, towards the North Odisha-West Bengal coast. Associated with this, an MCS was developed. This system passed through Central India between 14-17 September 2023, and continued to move in the west-northwestward direction, causing isolated EREs, floods, and flood-like situations in various regions. This LPA weakened on 17 September, as it reached Gujarat (IMD 2023f, g). An approximate track of this system movement is shown by a red line in Fig. 1a. Significant rainfall recorded by the Automatic Weather Stations (AWS) in various regions of Madhya Pradesh as per the reports are shown in Fig. 1c (IMD 2023f, g) and the corresponding station locations are marked in Fig. 1b. These stations can be seen to be clustered more around the track, as marked by the black dots in Fig. 1a.

The synoptic conditions associated with the event during the period 15–18 September 2023, 00:00 UTC, from the fifth generation European Centre for Medium-Range Weather Forecasts (ECMWF) atmospheric reanalysis (ERA5) data, confirmed that the event was a low-to-mid-level monsoon low-pressure system, accompanied by an MCS. The system exhibited an organized cyclonic circulation at 500 hPa, as shown in Fig. S1 in supplementary material, and a trough-like structure was predominant at 300 hPa (Fig. S2), which is commonly associated with MCSs. At 500 hPa, divergence dipoles were observed as can be seen in Fig. 2, strengthening and weakening over time, indicating the evolution of the MCS. Divergence dipoles were evident at 300 hPa on 15 September 2023, 12:00 UTC and 16 September 2023, 00:00 UTC, around which the maximum rainfall occurred over the study region (Fig. S3). The vorticity analysis further supports the evolution of the system. Higher values of vorticity

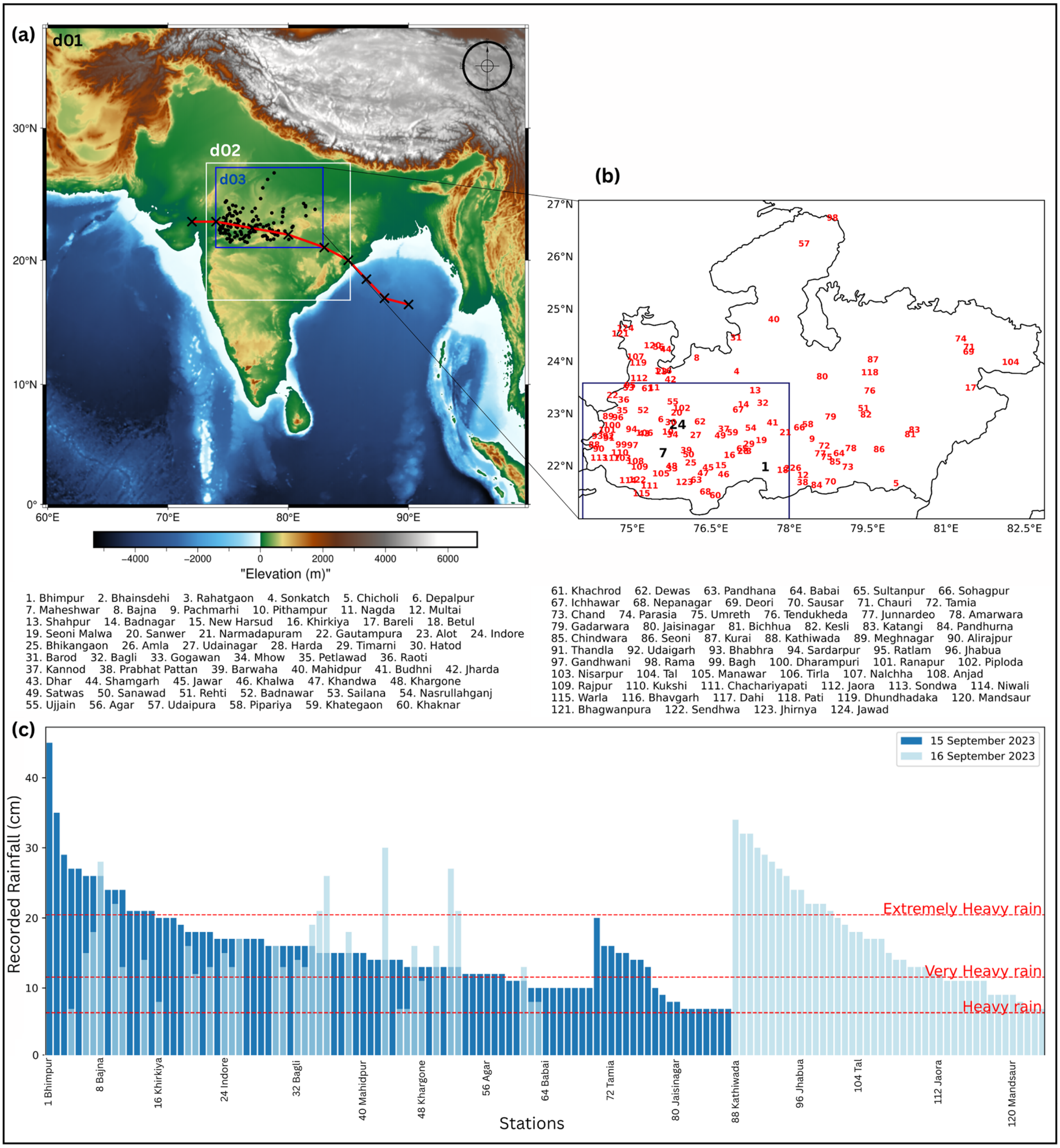

Fig. 1 **a** WRF domain configuration with triple-nested domains d01 (18 km, 234 × 234), d02 (6 km, 211 × 202), and d03 (2 km, 469 × 352) with topography created using PyGMT(Uieda et al. 2021). Approximate track of the system is shown as a red line. Locations of the Automatic Weather Stations (AWS) that recorded significant rainfall over Madhya Pradesh (d03) are marked with black dots and labeled in **b**. **c** Presents the amount of rainfall received by these stations for 15 and 16 September 2023, as per the IMD report (IMD 2023f, g). The classification of different rainfall types are based on IMD (2023a)

were observed at the center of the depression at 500 hPa levels (Fig. S4). Stronger and more localized vorticity is observed at 300 hPa on 15 September 2023, and can be seen to be weakening after 16 September 2023 18:00 UTC (Fig. S5). The wind speed analysis reveals an intensification at 850 hPa with stronger and maximum wind speed near the center of depression that can be seen on 16 September 2023 (Fig. S6). This indicates low-level convergence and

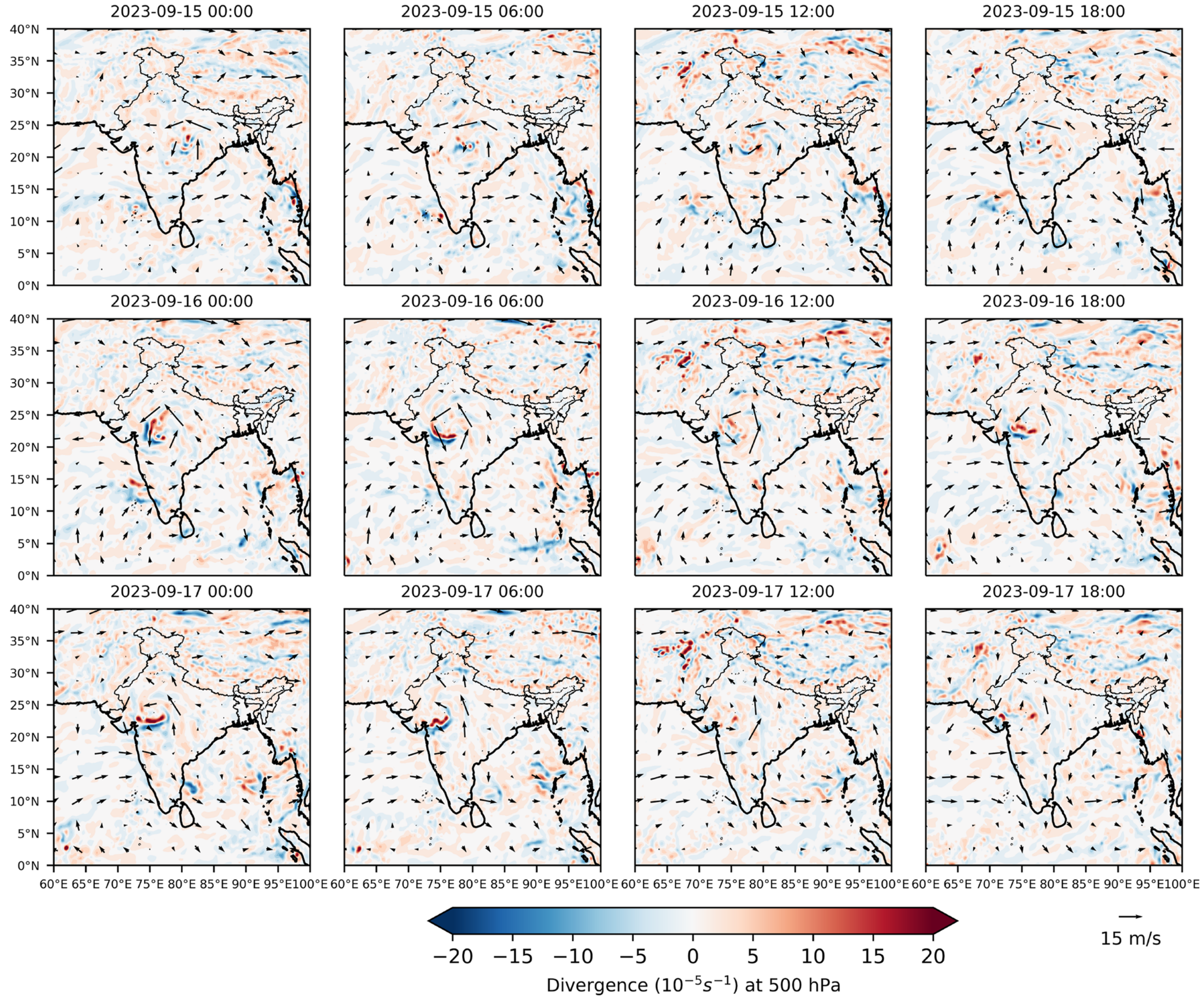

Fig. 2 Spatial distribution of wind divergence at 500 hPa, overlaid with wind vectors that indicate the cyclonic circulation

moisture transport. Similarly, at 500 hPa significantly high wind speed was observed near the center of the system that reflects the vertical coherence and strength of the system (Fig. S7). The system progressively weakens and dissipates, as indicated by the weakening of circulation, disappearance of divergence dipoles, and decrease in the wind speed and vorticity values. The model simulations are compared with these understandings about the system to see if the simulations are able to capture the same.

Model description

Model configuration

The Advanced Research WRF (WRF-ARW) version 4.5.1 is used to create the simulations for the study (Skamarock et al. 2021; Hatheway et al. 2023). The ARW core of the model consists of a set of non-hydrostatic primitive equations with an option for using hydrostatic in run-time. It has horizontal discretization given by the Arakawa-C grid staggering, a hybrid vertical coordinate, and time-integration by the 3rd-order Runge–Kutta scheme. Simulations are made in a triple-nested domain configuration as shown in Fig. 1a, with the third domain (d03) covering the whole of Madhya Pradesh. Analysis data from National Centers for Environmental Prediction (NCEP) final (FNL) operational global analysis and forecast datasets at $0.25^\circ \times 0.25^\circ$ resolution are used as initial (ICs) and lateral boundary conditions (BCs) at every 6 h. The detailed model configuration is provided in Table 2.

Table 2 Model configuration for the study

Model Configuration	Description		
WRF core	ARW		
Projection	Mercator		
Domains	d01	d02	d03
Horizontal resolution	18 km	6 km	2 km
Number of Grids	234 × 234	211 × 202	469 × 352
Domain Dimensions	0° - 36.96°N 59.85° - 99.7° E	16.85° - 27.43°N 73.19° - 85.16°E	21° - 27.09°N 73.97° - 82.88°E
Number of Vertical levels	44		
Model Top Height	50 hPa		
Terrain Elevation	USGS Topography Data		
Land Use	MODIS 21 categories		
Feedback	On		
Simulation Period	00:00 UTC 15 - 00:00 UTC 18 September 2023		
Spin-up Period	6 h		
Temporal Resolution	1 h		

Table 3 Configurations of MP, CU, and PBL schemes

Set	MP scheme	CU scheme	PBL scheme
set 1	Goddard	KF	MYJ
set 2	WSM6	–	YSU
set 3	Goddard	BMJ	YSU
set 4	WSM6	KF	YSU
set 5	WSM6	BMJ	YSU
set 6	Goddard	-	YSU
set 7	Goddard	KF	YSU
set 8	Thompson	KF	YSU
set 9	Thompson	BMJ	YSU
set 10	Thompson	BMJ	MYJ
set 11	WSM6	BMJ	MYJ
set 12	Goddard	BMJ	MYJ
set 13	Thompson	KF	MYJ
set 14	WSM6	KF	MYJ
set 15	WSM6	-	MYJ
set 16	Goddard	-	MYJ
set 17	Thompson	-	MYJ
set 18	Thompson	-	YSU

Simulation design

18 simulations are designed as described in Table 3 considering 2 PBL schemes, 3 CU schemes and 3 MP schemes. The choice of the schemes are based on the literature as discussed before. Rainfall and other associated parameters from each simulation are analyzed to see the performance of the model in capturing the event realistically. Details of the schemes used are mentioned in Appendix A.

Datasets

To evaluate the model performance, rainfall parameter along with horizontal winds, temperature and relative humidity (hereafter RH) are considered. While the model simulations are at a high spatial resolution of 2 km, the evaluation is carried out against GPM IMERG and IMDAA, of lower spatial resolutions $0.1° \times 0.1°$ and $0.12° \times 0.12°$, respectively, which are considerably coarser resolutions. The model outputs are resampled using the nearest neighbor method to match the resolutions of GPM IMERG and IMDAA. However, it should be noted that this upscaling has several challenges, such as potentially smoothening out the local extremes captured by the model and slightly altering the rain/no-rain area. Such discrepancies can impact the model performance during evaluation, which is not necessarily due to the model bias. The datasets used for the evaluation are described below:

GPM IMERG

The Integrated Multi-satellitE Retrievals for Global Precipitation Measurement (GPM IMERG) provides high-resolution $(0.1° \times 0.1°)$ precipitation data estimated from the GPM mission at temporal resolutions of 30 min, 1 day, and 1 month (Huffman et al. 2015). Based on the type of processing, there are three variants for IMERG-Early Run (≈ 4 hour latency), Late Run ($\approx 12 - 14$ hour latency), and Final Run (≈ 3.5 months latency) - with the Final Run specifically designed for research use. It integrates monthly Global Precipitation Climatology Centre (GPCC) gauge data and other high-quality fields from reanalysis datasets like Modern-Era Retrospective analysis for Research and Applications, Version 2 (MERRA-2) and ERA5. A month-to-month spatially varying bias adjustment is applied, ensuring that each half-hourly estimate will reflect the best possible calibration for that month. Consequently, this study considers hourly rainfall data from the IMERG Final Run (V07) for evaluating model-simulated precipitation.

IMDAA reanalysis

The regional dataset Indian Monsoon Data Assimilation and Analysis (IMDAA) is a reanalysis dataset developed by the National Centre for Medium Range Weather Forecasting (NCMRWF) and IMD in collaboration with the Met Office (MO), UK. The dataset is prepared using ERA-interim (ECMWF replaced this dataset with its successor ERA5 in 2019) as the initial and lateral boundary conditions and is run on the U.K. Met Office Unified Model. IMDAA provides single- and pressure-level data at a high spatial resolution of $0.12° \times 0.12°$ (Rani et al. 2021). The single-level variables are available at a temporal resolution of one hour, whereas the pressure-level variables are available every three hours. To validate other parameters from the model simulations, this dataset is being used in this study.

Evaluation

Continuous and categorical statistical indices are used in this study, along with the calculation of Fractional Skill Score (FSS) to assess the consistency and overall performance of the models in simulating the event. Continuous statistical indices such as root mean square error (RMSE), mean absolute error (MAE), mean bias (MB), and correlation coefficient (CC) are calculated for the aforementioned variables. The model performance in capturing rainfall is also evaluated using categorical statistical indices, such as Probability of Detection (POD), Critical Success Index (CSI), False Alarm Ratio (FAR), and Equitable Threat Score (ETS). These indices are calculated based on the hits, misses, false alarms and correct negatives as shown in the contingency table in Fig. 3. A 0.1 mm/h threshold is used following common practices in high-resolution model validation. The equations for these indices are provided in Appendix B.

The hourly rainfall from the simulations are compared to analyze the spatial and temporal variations. To study the temporal variations, averaging over the domain is considered, whereas for studying the spatial variations, a cell-by-cell comparison is carried out by averaging over time. To capture the spatial similarities, FSS test is carried out at a threshold of 0.1 mm/h (Roberts and Lean 2008). To evaluate how well these models are in capturing the HREs, a 90 percentile threshold is also applied.

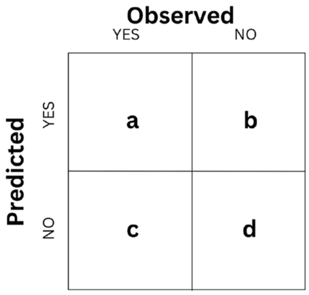

	Observed YES	Observed NO
Predicted YES	a	b
Predicted NO	c	d

Fig. 3 Contingency table illustrating the distribution of observed and simulated events beyond a specified threshold, categorized as Hits (a), Misses (b), False Alarms (c), and Correct Negatives (d)

Results

Performance of WRF simulations in capturing the rainfall

Temporal characteristics of rainfall

The domain-averaged hourly rainfall from GPM IMERG, represented by the solid black line in Fig. 4, indicates that the maximum rainfall over d03 occurred around 12:00 UTC on 15 September 2023. A secondary increase in rainfall around midnight on 16 September 2023 can be observed, which declines gradually, leading to two distinct peaks. The time series analysis of 18 simulations are displayed in sets of 3 in Fig. 4, where columns 1 and 2, and rows 1, 2, and 3, have simulations made with YSU and MYJ PBL, and WSM6, Goddard, and Thompson MP schemes, respectively. Those in dash-dot green lines have KF used in the innermost domain, dashed blue lines are those with no CU and dotted red are those with BMJ as CU. All simulations display a temporal delay in capturing the rainfall along with an underestimation. Additionally, it can also be noted that most of the simulations are unable to capture the second peak properly. However, Sets 13 (KF + WSM6 MP + MYJ PBL) and 14 (KF + Goddard MP + MYJ PBL) are able to capture this quite well. The influence of different combinations of physical parameterization schemes can clearly be seen in this figure. Simulations run with Goddard MP and YSU PBL exhibit better temporal matching in capturing the initial peak of rainfall compared to others. Simulations with BMJ CU are consistently underperforming and are capturing an unrealistic third peak on 17 September 2023. Although Set 6 (No Cu + Goddard MP + YSU PBL) captures the trend better than Set 7 (KF + Goddard MP + YSU PBL), in general, simulations with KF in the innermost domain are able to capture the peaks better than the one with CU turned off in the innermost domain.

Statistical analysis corresponding to this is presented in Fig. 5. Although Sets 13 and 14 are able to capture the trend better than others, the positive MB indicates their overestimation. On the other hand, all other simulations are underestimating, as indicated by their negative MB values. Although no single combination consistently outperformed others across all four metrics (MB, RMSE, MAE, and CC), comparative analysis indicates that Set 4 (KF CU+YSU PBL+ WSM6 MP) and Set 8 (KF CU+YSU PBL+ Thompson MP) performed better. Set 4 recorded an MB of −0.021 mm/h, the lowest RMSE (0.297 mm/h), MAE of 0.230 mm/h, and CC of 0.896. Set 8 achieved the lowest MB (0.002 mm/h), with RMSE of 0.33 mm/h, MAE of 0.253 mm/h and CC of 0.865.

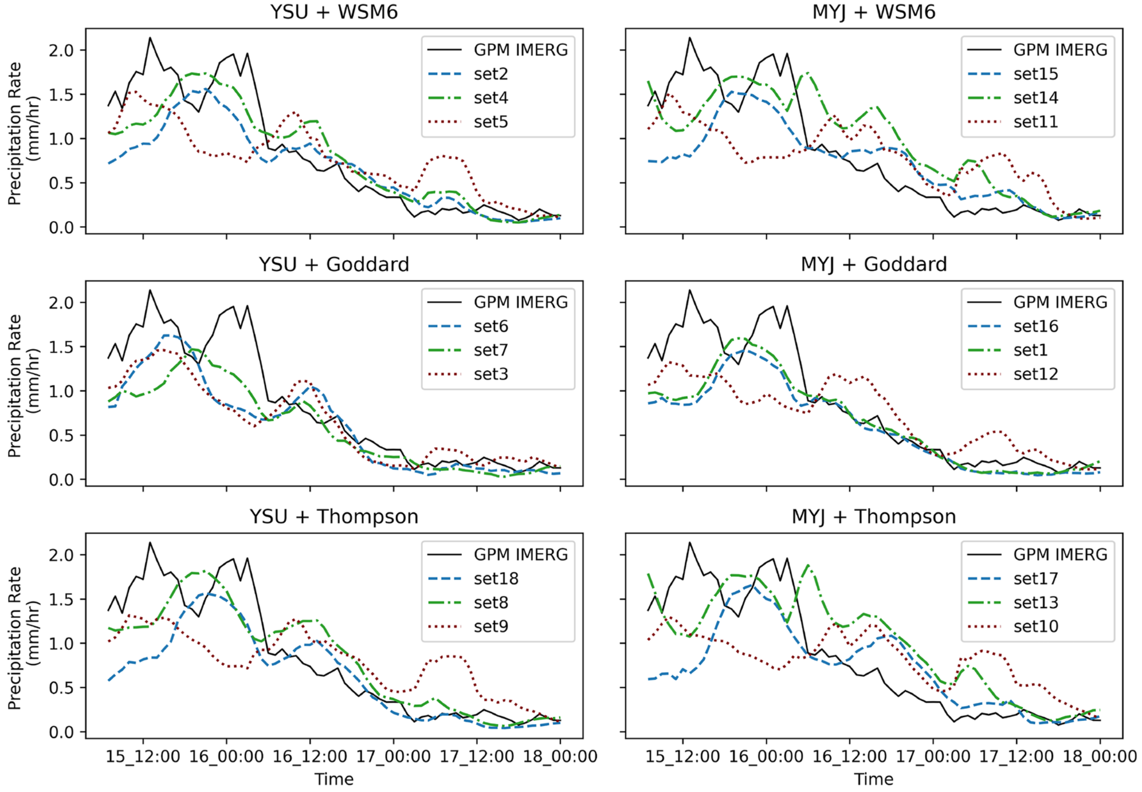

Fig. 4 Time series analysis of rainfall over d03 from 06:00 UTC on 15 September to 00:00 UTC on 18 September 2023. The solid black line represents the rainfall from GPM IMERG. Dash-dot green lines represents simulations with KF used as CU, dashed blue lines are those with CU turned off and dotted red lines are those with BMJ as CU

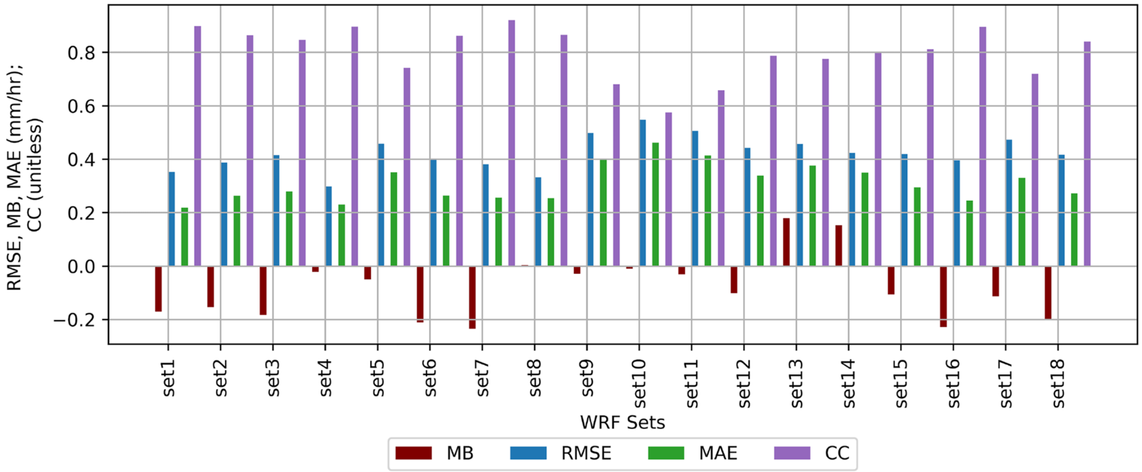

Fig. 5 MB, RMSE, MAE and CC for all simulations

Spatial characteristics of rainfall

Cell-by-cell analysis was performed to calculate the spatial MB, RMSE and MAE for each simulation and the calculated values for each set are presented in the Fig. 6a-c. The MB values range across the sets from −4.74 to 10.17 mm/h, with the minimum bias range observed for Set 8 (−2.8-3.77 mm/h), followed by Set 15 (−3.01-3.61 mm/h) and Set 1 (−3.56-3.13 mm/h). While most simulations have a maximum MB up to 4 mm/h, Sets 13 and 14 highly overestimates rainfall over a small localized region. These regions also have high values of MAE and RMSE. MAE values range from 0 to 11.46 mm/h across all the sets. Set 16 has the least MAE range (0-5.62 mm/h), followed by Sets 7 (0-6.04 mm/h) and 6 (0-6.41 mm/h). In terms of RMSE, Set 1 (0-11.62 mm/h)

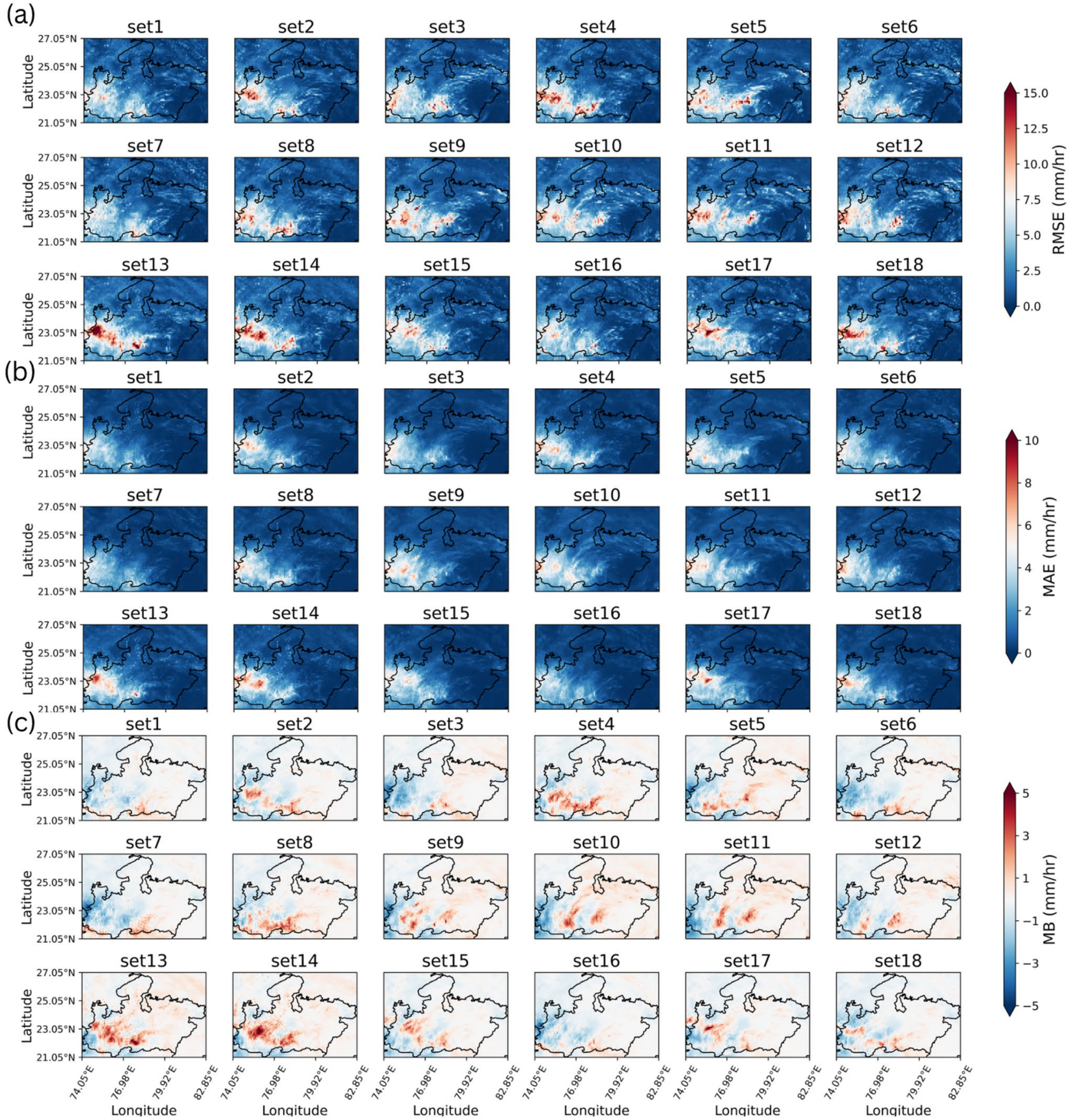

Fig. 6 Cell-by-cell **a** RMSE (mm/h), **b** MAE (mm/h) and **c** MB (mm/h) for each simulation

performs the best, followed by Set 7 (0-12.6 mm/h) and Set 6 (0-12.77 mm/h).

To capture the spatial similarities in the model, FSS is further computed. With 0.1 mm/h as the threshold and a window scale of 3 units, Set 8 was found to perform best with a score of 0.62, followed by Set 1 (0.61). But upon varying the threshold to 90 percentile to capture the HRES and EREs, Set 1 was found to perform better with a score of 0.58, followed by Set 16 (0.56) as shown in Table 4.

Sensitivity to physical parameterizations

The analysis treats all grid cells across time as a single ensemble and the corresponding scores are shown in Fig. 7. No single scheme performed well in all tests. While Set 8 had the least MB of -5×10^{-4} mm/h and highest CSI of 0.36 mm/h, Set 1 had the lowest RMSE of 2.80 mm/h. Set 16 scored the lowest MAE, whereas Set 13 had the highest POD score, followed by Sets 10 and 8. FAR was lowest for

Table 4 Spatial validation statistics (RMSE, MAE, MB) and Fractional Skill Score (FSS) for all simulations

Set	RMSE (Min–Max) mm/h	MAE (Min–Max) mm/h	MB (Min–Max) mm/h	FSS (0.1 mm/h)	FSS (90 percentile)
Set 1	0.01–11.62	0.00–7.26	–3.56 to 3.13	0.61	0.58
Set 2	0.01–17.02	0.00–7.83	–3.49 to 4.16	0.59	0.55
Set 3	0.01–18.50	0.00–6.74	–4.70 to 4.49	0.48	0.42
Set 4	0.01–17.57	0.00–7.46	–2.72 to 5.52	0.60	0.52
Set 5	0.02–18.87	0.01–7.87	–4.86 to 4.13	0.51	0.45
Set 6	0.00–12.77	0.00–6.41	–3.43 to 3.53	0.49	0.46
Set 7	0.00–12.60	0.00–6.04	–5.31 to 3.75	0.55	0.53
Set 8	0.03–14.16	0.01–7.01	–2.80 to 3.77	0.62	0.53
Set 9	0.05–18.90	0.01–7.63	–4.29 to 5.03	0.52	0.42
Set 10	0.03–12.76	0.01–7.10	–4.06 to 3.71	0.52	0.36
Set 11	0.04–17.54	0.01–7.37	–3.64 to 4.68	0.51	0.37
Set 12	0.01–19.56	0.00–7.29	–3.67 to 3.70	0.53	0.45
Set 13	0.08–28.74	0.03–11.46	–3.37 to 10.17	0.56	0.44
Set 14	0.03–17.66	0.01–8.88	–3.30 to 6.40	0.56	0.46
Set 15	0.01–14.00	0.00–6.91	–3.01 to 3.61	0.59	0.53
Set 16	0.01–13.45	0.00–5.62	–4.74 to 3.63	0.57	0.56
Set 17	0.00–19.26	0.00–9.93	–3.46 to 5.80	0.57	0.51
Set 18	0.00–16.24	0.00–7.41	–2.99 to 4.22	0.55	0.54

Set 2, followed by Sets 1, 4 and 8. Sets 4 and 1 followed Set 8 in scoring high values of CSI. ETS, on the other hand, was highest for Set 7, followed by Sets 1 and 16.

Performance of WRF simulations in capturing horizontal winds, temperature and RH

Resampled three hourly horizontal winds, temperature and RH from the 18 simulations are evaluated using the IMDAA reanalysis data and the corresponding error statistics is presented using a Taylor Diagram as shown in Fig. 8. In Fig. 8 (c), it can be seen that all 18 simulations perform similarly in simulating the temperature and also similar to the temperature from IMDAA. All simulations have a CC of 0.99 and RMSE values lies between 1.34-1.53 K. The standard deviation (SD) of all the simulations can be seen in the figure to be very close to that of the observation. The MAE values ranges between 1.06-1.22 K with Set 6 performs better than others, whereas, the MB values ranges between −0.10 - −0.37 K with Set 8 performs best. All simulations were able to capture the temperature variable over d03 very well.

On the other hand, there are variations in simulating horizontal winds and RH by these models, as can be seen in Fig. 8a, b, respectively. From Fig. 8a it can be seen that the SD of all the simulations are slightly less than the observations, indicating that the models tend to capture lower wind variability. The CC values vary between 0.60-0.69 and the RMSE values in the range of 3.51-4.03 m/s. The MAE values of these simulations range from 2.63-3.09 m/s and the MB values range from −0.60 - −1.26 m/s. Set 1, followed by Set 16 is found to have the highest CC, and the lowest RMSE and MAE values in capturing the horizontal winds. Sets 13 and 14 are found to have the least deviation among the sets compared to IMDAA.

The SD values for all the simulations in Fig. 8b indicate that the RH simulated by the models captures higher variability. All simulations also exhibit better spatial pattern similarity with CC values ranging between 0.72 to 0.79 and the RMSE values ranging between 18.67−22.04 %. The MAE and MB values are between 13.69-16.00 % and −2.08 - −8.97 %, respectively. Sets 3, 5, 9, 10, 11 and 12 captures more RH variability than others. They have a lower value of CC, and more deviation than other simulations. These are the six simulations designed with BMJ as the CU. This supports that BMJ does not perform well in capturing the event in this case. Simulations with CU as KF, turned on and off in the innermost domain, performs somewhat similar. Sets 13, 8 and 14 has the least deviation, while Set 4 has the highest CC. These four simulations are designed with KF turned on in the innermost domain.

While Set 1 performed best in capturing the spatial distribution of rainfall in the FSS test, Set 8 performed best in capturing the temporal pattern of rainfall. Since no single combination of schemes performed best across all the metrics, a ranking approach as mentioned in Evans et al. (2012) was adopted, where the inverse of certain metrics (CC, POD, CSI and ETS) are taken followed by normalization of all the metrics. A mean across the metrics is taken for each simulation, and the scheme combination with the lowest score is considered to have the highest skill. The rank of the schemes together with the corresponding scores are provided in Table 5. In this ranking approach, Set 8 was found to have an overall best performance, followed by Sets 4 and 1. These three are schemes with KF used as the CU scheme in the innermost domain. There are also other ranking methods like the multiplicative ranking method as mentioned in Evans et al. (2012). The multiplicative method

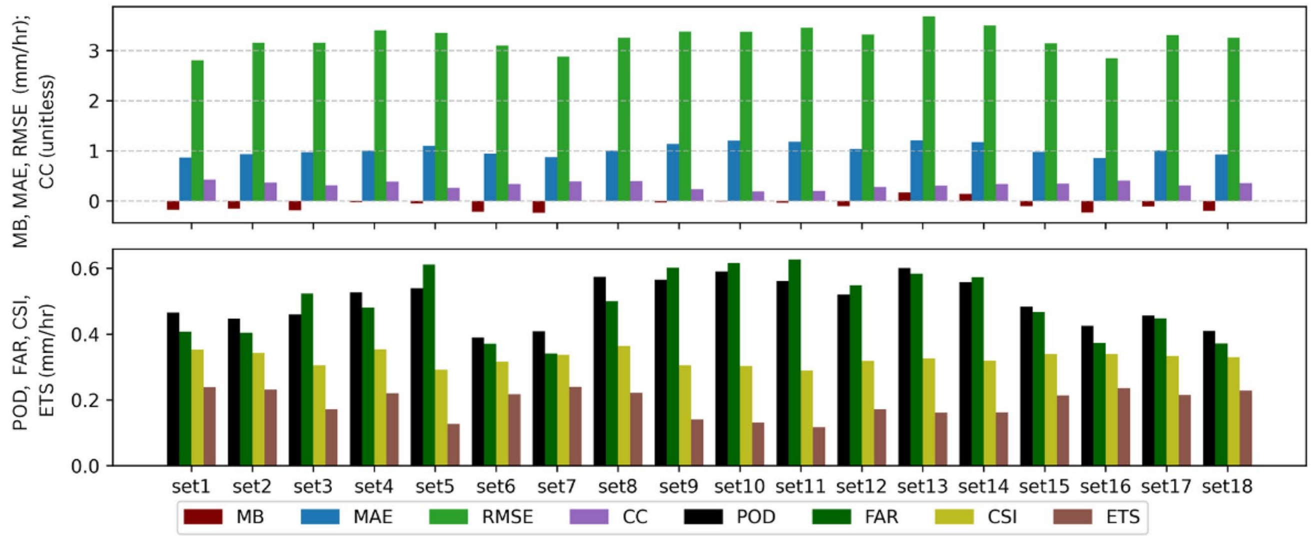

Fig. 7 Continuous and categorical indices calculated to understand the overall performance of simulations in capturing the rainfall

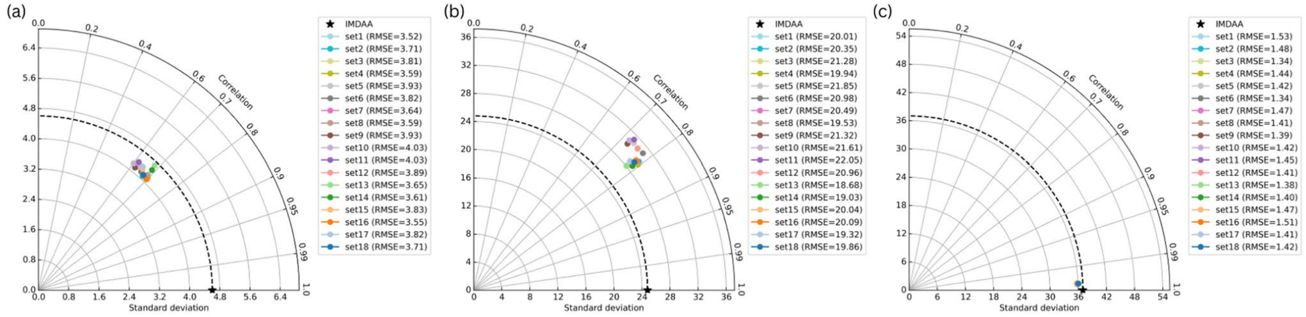

Fig. 8 Taylor diagram representing the deviation, RMSE (K) and CC of **a** horizontal wind speed (left), **b** RH (middle) and **c** temperature (right from the 18 different simulations with respect to IMDAA

Table 5 Model ranking based on performance score

Rank	Set	Score	Rank	Set	Score	Rank	Set	Score
1	Set 8	0.679	7	Set 16	0.789	13	Set 3	0.800
2	Set 4	0.710	8	Set 18	0.792	14	Set 12	0.803
3	Set 1	0.750	9	Set 9	0.794	15	Set 10	0.808
4	Set 15	0.752	10	Set 7	0.796	16	Set 6	0.828
5	Set 17	0.753	11	Set 14	0.796	17	Set 11	0.831
6	Set 2	0.767	12	Set 13	0.797	18	Set 5	0.836

also yielded a similar result in terms of the ordering of the schemes. Here Set 8 exhibited better performance as well. It should be, however, keep in mind that depending on the tests carried out as well as on the type of ranking approach followed, the "best-performing set" may vary.

Impact of lead time in simulating the MCS

MCSs being rapidly evolving systems, the lead times of the simulation can have an impact on the spatio-temporal distribution of rainfall. Since all 18 simulations had a temporal delay in capturing rainfall, simulations with different lead times were also studied. Here additional four simulations with Set 8 were made with the initial times as 14 September 2023 18:00 h (12 h lead time; Run 1, hereafter), 14 September 2023 12:00 h (18 h lead time; Run 2, hereafter), 14 September 2023 00:00 h (30 h lead time; Run 3, hereafter)and 13 September 2023 12:00 h (42 h lead time; Run 4, hereafter). However, the analysis indicated that although the positions of the peaks slightly varied in time, they all exhibited a temporal delay as shown in Fig. 9. Cell-by-cell analysis from Fig. 10 indicated that the spatial errors increased with more lead times. FSS analysis indicated that Set 8 (with 6 h lead time) performed better in capturing the rainfall at both

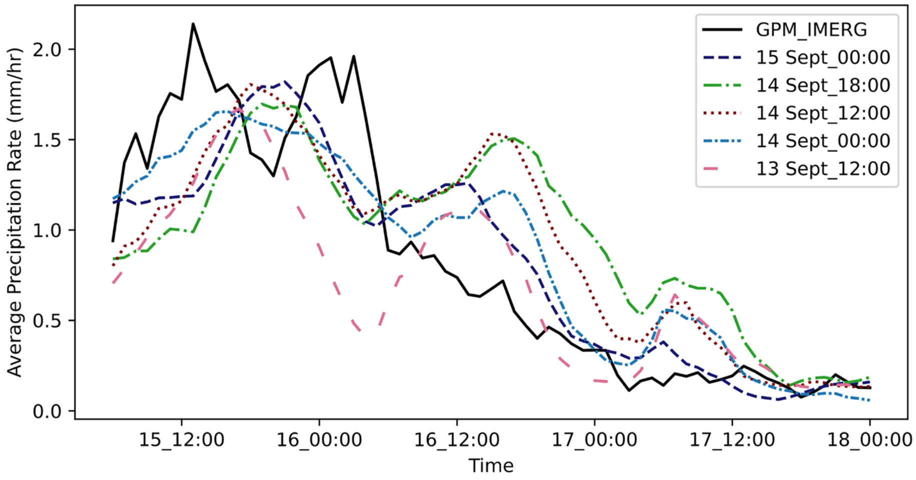

Fig. 9 Time series analysis of rainfall over d03 from simulations with different lead times during 06:00 UTC 15 September 2023-00:00 UTC 18 September 2023. Each simulations are labeled with their respective initialization time. The solid black line represents the GPM IMERG rainfall, dashed dark blue lines represent Set 8 (00:00 UTC 15 September 2023), dash dot green line represent Run 1 (18:00 UTC 14 September 2023), dotted maroon line represent Run 2 (12:00 UTC 14 September 2023), short dash dot blue line represent Run 3 (00:00 UTC 14 September 2023) and spaced dash pink line represent Run 4 (12:00 UTC 13 September 2023)

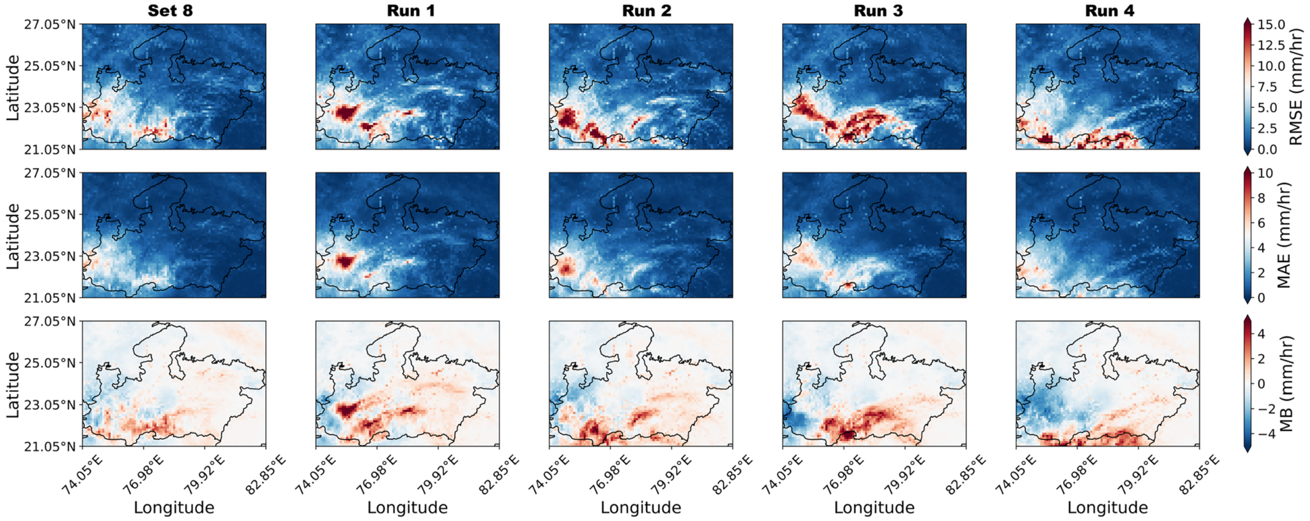

Fig. 10 Cell-by-cell RMSE (mm/h), MAE (mm/h) and MB (mm/h) from Set 8 and Runs 1-4

0.1 mm/h and 90 percentile thresholds than all other lead times. The composite scoring technique also indicates the best model is with 6 h lead time with a score of 0.55, followed by Runs 3(0.72), 2(0.83), 4(0.89) and 1(0.95).These results indicate that the temporal delay observed is not related to lead time but could be due to some other factors.

Diagnosis of the event from 15 to 17 September 2023

Synoptic conditions

The synoptic conditions associated with the event for 15–17 September 2023 are analyzed from the outermost domain of the model simulation Set 8. The movement of the system can be seen by the depression observed in the mean sea level pressure (MSLP) (Fig. S8). The center of the depression can be seen to be over Chhattisgarh-Madhya Pradesh border at 00:00 UTC 15 September 2023. The center of the system is seen to be moved towards the South-Central regions of Madhya Pradesh at 00:00 UTC 16 September 2023. Weakening of the depression and dissipation can be observed on 17 September 2023. An organized cyclonic circulation can be observed at 500 hPa (Fig. S9) and at 300 hPa, a trough-like structure dominates, although a very weak depression is evident on 15 and 16 September 2023 (Figure S10). These are in agreement with the observations from ERA5. The intensification of the wind speed near the depression can be seen in Figs. S8 and S10. The simulated wind speed although spatially correlated with ERA5, it produced slightly weaker winds. The strength of other variables diagnosed varied across the simulations and, in general, simulations with KF CU in the innermost domain captured them better than others.

Divergence dipoles, which are a signature of MCS events can be observed at 500 hPa and 300 hPa. However, there is a time delay in capturing these signatures when compared with ERA5. Strong and more localized divergence dipoles are observed at 500 hPa as presented in Fig. 11. At 300 hPa, strong divergence dipoles are captured by ERA5 at 12:00 UTC 15 September 2023 while Set 8 captures this at 18:00 UTC 15 September 2023. The vorticity generated by the model is more localized and stronger than that produced by ERA5. Positive vorticity values can be observed at 300 hPa on 15 and 16 September 2023. The integrated vertical moisture transport (IVT) indicates the amount of horizontal moisture flux that is integrated up to 300 hPa, which helps in quantifying how much water vapor is being transported into a region. The IVT from the model is presented in Fig. 12 where the moisture reaches upto $\approx 1200\ \mathrm{kg\,m^{-1}\,s^{-1}}$. Maximum IVT is observed at 00:00 UTC 16 September 2023, time around which rainfall was also quiet significant. IVT from ERA5 was however upto $\approx 1400\ \mathrm{kg\,m^{-1}\,s^{-1}}$ (Figure S15). This underestimation of IVT from model can be due to the lesser vertical transport of moisture due to the weaker wind speed simulated in comparison to ERA5.

From analyzing the synoptic conditions, it was understood that the model is able to capture the synoptic environment associated to the event. Features that indicate the presence of an MCS is also being captured although they are not as prominent as that noted from ERA5.

Characteristics of winds

The domain-averaged time-height analysis of horizontal and vertical winds can help in understanding the key dynamical features associated with the event. First row of Fig. 13 presents the time-height analysis of vertical wind velocity from the best performing model sets - Set 8, Set 4 and Set 1, along with velocity from IMDAA. On the first day, around the time of maximum precipitation, strong updrafts are observed.

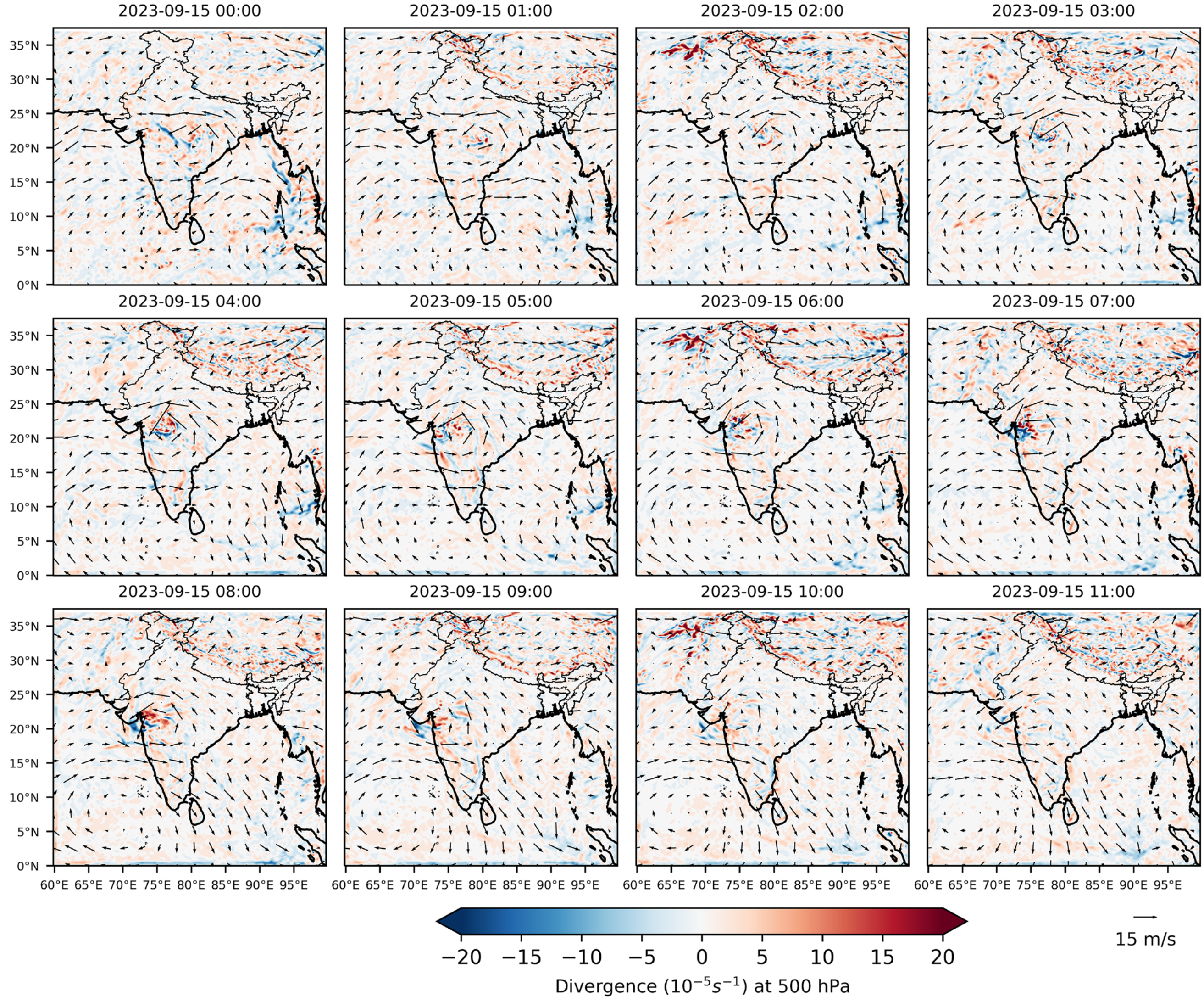

Fig. 11 Wind Divergence at 500 hPa simulated from WRF from Set 8 (Thompson MP + YSU PBL + KF CU)

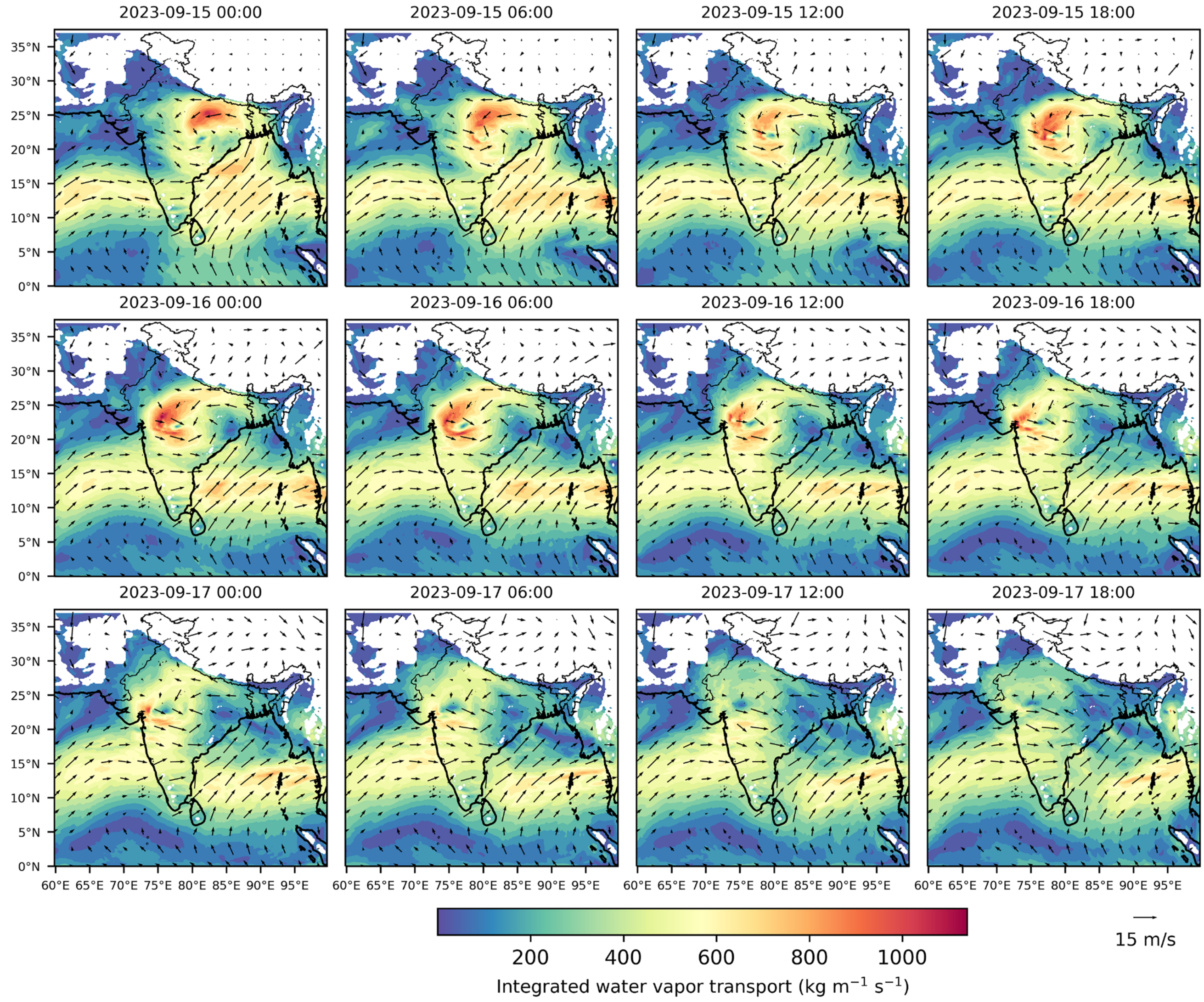

Fig. 12 Integrated Vertical moisture Transport (IVT) from Set 8, overlaid by quiver plot of winds at 850 hPa

From Set 8, the vertical velocity is found to peak around 12.5 km altitude and remains strongly positive up to around 15 km. From there, up to around 17.5 km, weaker yet still positive values are observed and negative values thereafter. This suggests the presence of deep convection reaching the upper troposphere, which supports the heavy rainfall that was observed during this period. This is in agreement with the vertical velocity from IMDAA although the reanalysis dataset has more intense positive vertical velocity.

A comparison of Sets 8 and 18 reveals that using KF as the CU scheme in the innermost domain (as in Set8) greatly strengthened the updrafts. Interestingly, simulations using the BMJ cumulus scheme produced stronger updrafts on the second day and even exhibited a continued ascent on the third day, which corresponds to additional peaks in the simulated rainfall. However, such rainfall was not observed, which indicates that these simulations may be overestimating vertical motion and producing spurious convection. This suggests that the BMJ scheme not suitable for this particular event. The supporting figure is provided in supplementary material Fig. S16. The horizontal wind analysis carried as shown in second row of Fig. 13, indicated the presence of very strong winds. Near to 17.5 km altitude, intense wind speed can be observed whose intensity decreases over time with speed increasing between 12-15 km altitude. Intense wind speed can be observed up to around 10 km, with the speed intensifying near to 00:00 UTC 16 September 2023. The speed can be found to be significantly less after 12:00 UTC 17 September 2023. Lesser yet strong winds can be observed between 10-12 km on 15 and 16 September 2023 from Set 8, although the speed observed is less intense in Sets 1 and 4. Similar features can be seen from the IMDAA simulations as well, although it has stronger winds within $\approx 10\text{km}$ and the simulated upper level winds are slightly

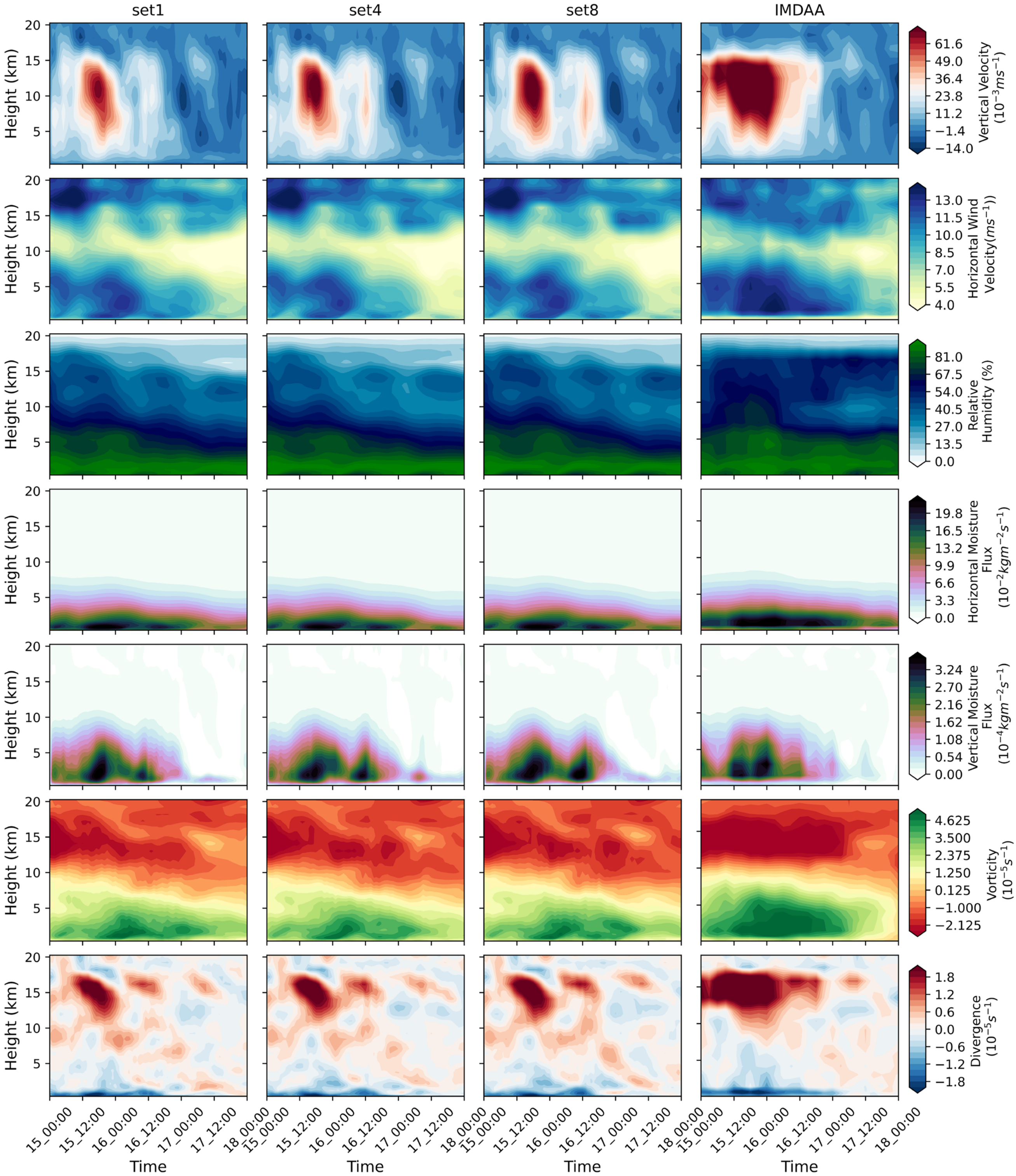

Fig. 13 Time-Height variation of (from top to bottom rows): Vertical Velocity ($10^{-3}\mathrm{ms}^{-1}$), Horizontal Wind Velocity (ms^{-1}), Horizontal Moisture Flux ($10^{-2}\mathrm{kgm}^{-2}\mathrm{s}^{-1}$), Vertical Moisture Flux ($10^{-4}\mathrm{kgm}^{-2}\mathrm{s}^{-1}$), Vorticity ($10^{-5}\mathrm{s}^{-1}$) and Divergence ($10^{-5}\mathrm{s}^{-1}$) over d03 from Sets 1, 4, 8 and IMDAA

weaker. It can also be observed that simulations with MYJ PBL are simulating relatively stronger horizontal winds in comparison to their YSU PBL counterparts, as seen from Sets 8 and 13 (Figure S17). The effects of MP schemes in capturing the winds are also evident. For instance, Sets 4, 7 and 8 share the same PBL and CU schemes but differ in their microphysics: WSM6 in Set4, Goddard in Set7, and Thompson in Set8. At 00:00 UTC on 16 September 2023, a stronger horizontal wind feature can be seen in set 7 at $\approx 2.5\mathrm{km}$, which is not present in Sets 4 and 8. Vertically, the extent of the wind structure appears slightly longer in Sets 4 and 8. However, the differences are more prominent in MYJ-based sets. Sets 13 and 14 show strong winds at 15 km on the third day, which are not present in Sets 8, 4, 1 or 7. These differences underscore the importance of the combined effects of parameterization schemes.

Moisture flux, divergence and vorticity

Horizontal moisture flux peaks near the surface at the time of maximum rainfall as shown in the fourth row of Fig. 13, indicating low-level moisture convergence. In contrast, the vertical moisture flux (fifth row of Fig. 13) exhibits strong upward fluxes and near the time of peak rainfall, it reaches up to 10-12.5 km. A distinct region of strong positive divergence is observed between 12 and 17.5 km around the time of peak rainfall, especially during periods of enhanced vertical moisture flux. These findings are consistent with the corresponding data from IMDAA. Low-level convergence near the surface can also be supported by the strong negative divergence values as shown in the last row of Fig. 13. This supports deep convection activity. Strong positive vorticity is consistently observed near the surface, especially around the times of peak rainfall, indicating enhanced cyclonic circulation and convergence in the lower troposphere. Positive vorticity can be observed up to 10 km around the time of the first peak rainfall and a strong negative vorticity is present in the upper troposphere, typically between 12 and 17.5 km. The corresponding plots for each of the simulations are provided in the supplementary in Figs. S16–S22. Corresponding RH is also presented which indicates that during the first peak of rainfall, RH was very strong up to 10 km, and was prominent till ≈ 15-17.5 km. The RH from IMDAA is slightly stronger than the model simulations. Figures S16–S22 in supplementary presents these variables from all 18 simulations.

Hydrometeors and reflectivity

Time-height variation of different hydrometeors - cloud water (QCLOUD), rain water (QRAIN), graupel (QGRAUPEL), snow (QSNOW), ice (QICE) and water vapour (QVAPOR) - are analyzed to better understand the concentration of hydrometeors over d03 as shown in Fig. 14. Simulations using the Thompson MP scheme (like Set 8) produced very low QGRAUPEL. In contrast, simulations that were run with WSM6 MP scheme (like Set 4), were found to produce more QGRAUPEL near to the time of peak rainfall, and was primarily distributed between 5-15 km. QSNOW was most abundantly simulated by the Thompson scheme, followed by the Goddard. While for most simulations the QSNOW particles simulated was between 5-15 km, in some simulations like Set 8, the QSNOW simulated went up to 17.5 km. But the maximum QSNOW concentration remained in the range 7.5-12.5 km around the time of peak rainfall. QICE was found to be simulated by the Sets with Thompson MP at very low concentration near to the altitude of 12.5–15 km. However, those with Goddard MP (like Set 1) had more substantial QICE extending from around 7.5 to 17.5 km. It can be noticed that both ice and snow in Set 1 contributed to the maximum rainfall, however, in Set 8, the maximum rainfall corresponds to the snow in the atmosphere. In contrast, maximum rainfall in Set 4 is in presence of Graupel and ice. In all simulations, rain is detected below 5 km, but the signature of a melting layer is more pronounced in Set 4 and 8. While Set 4 and Set 8 show significant rain amount, Set 1 shows comparatively much lower rain amount below 5 km. Subsequently, the surface rain is maximum for Set 8 followed by Set 4 and Set 1.

QVAPOR had more higher values up to 2.5 km and was gradually decreasing with height in all the simulations. QCLOUD typically extended up to 7.5 km in all simulations, with Goddard MP producing stronger low-level cloud water, particularly below 2.5 km. QRAIN mostly remained confined within 5 km.

The supporting images are provided in the supplementary material Figs. S23-S29. These results highlight how the choice of microphysics scheme influences the phase and vertical extent of hydrometeors. Goddard and WSM6 schemes appear to simulate deeper and more robust ice and graupel processes, which are essential for understanding latent heat release and vertical momentum during deep convective events. Meanwhile, Thompson favors more snow production but weaker graupel and ice, which possibly influences the simulated intensity and structure of rainfall.

The vertical distribution and phase of hydrometeors, particularly QGRAUPEL, QSNOW, and QICE, play a crucial role in modulating the reflectivity, especially in deep convective systems. Since reflectivity primarily responds to the size and concentration of liquid and frozen particles, the patterns observed in the hydrometeor profiles will influence the vertical structure and intensity of the simulated reflectivity. Therefore, to further understand how different combination of schemes affect the organization and strength of

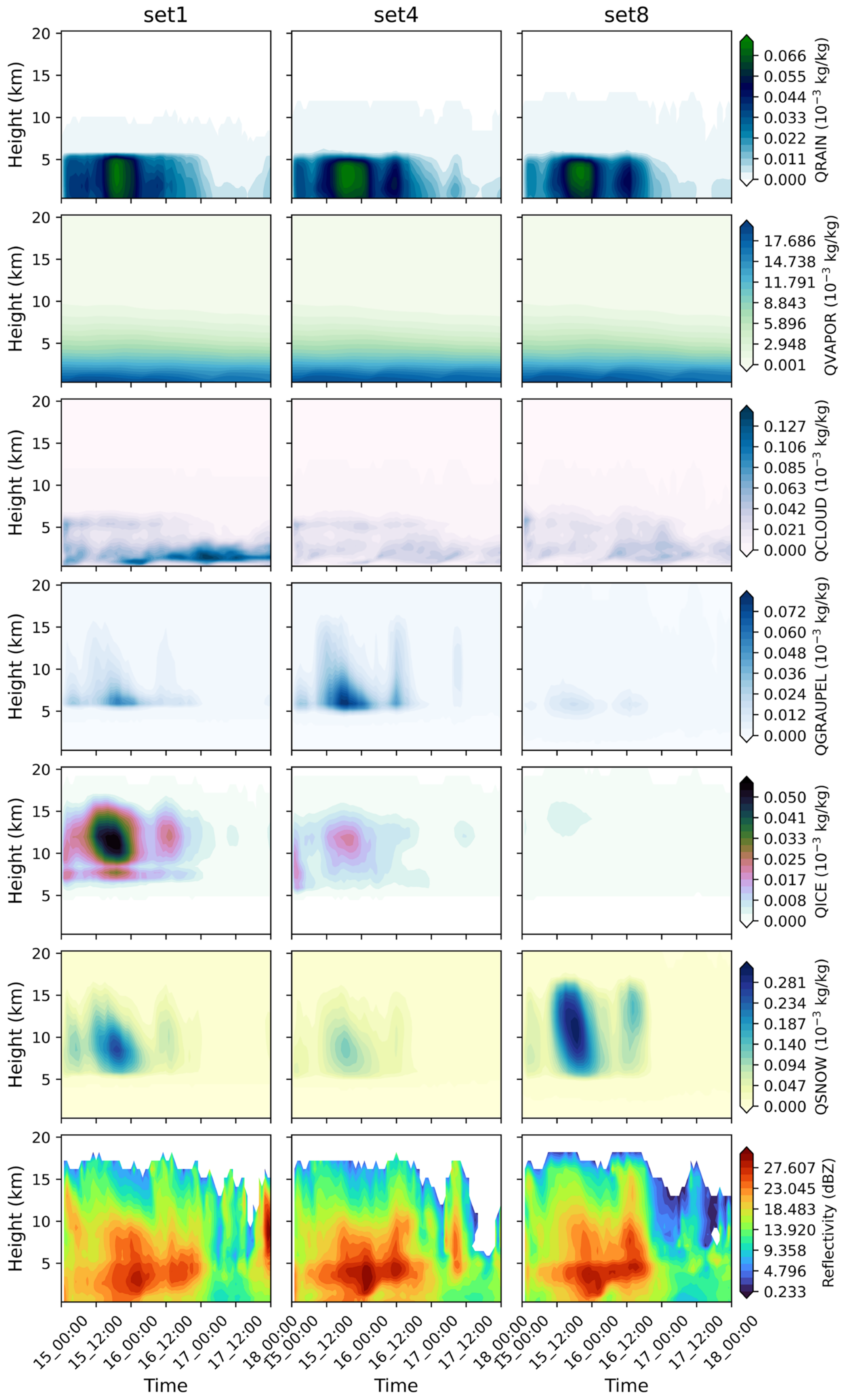

Fig. 14 Time-Height variation of the hydrometeors QRAIN (10^{-3}kg kg^{-1}), QVAPOR (10^{-3}kg kg^{-1}), QCLOUD (10^{-3}kg kg^{-1}), QGRAUPEL (10^{-3}kg kg^{-1}), QICE (10^{-3}kg kg^{-1}), QSNOW (10^{-3}kg kg^{-1}) and reflectivity (dBz) over d03, from Sets 1, 4 and 8

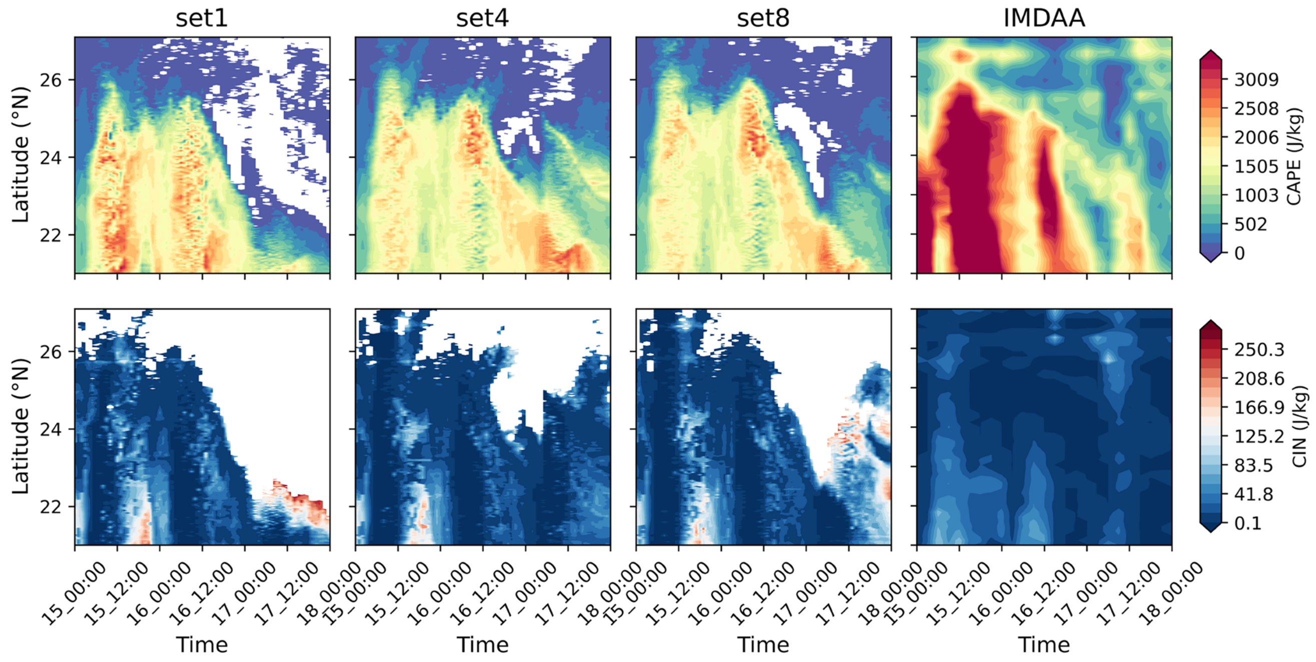

Fig. 15 Hovmoller diagram showing the spatial variation of CAPE (J/kg) and CIN (J/kg) over 75.84°E on d03

convection, the time-height variation of simulated reflectivity is analyzed as shown in the bottom row of Fig. 14. Sets 8 and 4 can be seen to be capable of representing the deep convection better than Set 1. Between 15 - 17 September 2023, the system is majorly seen to have high reflectivity between ≈3-5 km, and the high reflectivity can be seen up to ≈17.5 km near to the time of deep convection.

Evaluation of CAPE and CIN

To understand how the models represent the thermodynamic conditions associated with the event, parameters such as the convective available potential energy (CAPE) and convective inhibition (CIN) are analyzed. Hovmöller diagram is drawn for the two variables from Sets 1, 4, 8 and IMDAA as presented in Fig. 15 across the longitude of 75.84°E over d03. Since the system was found to move along the west-northwestwards direction, longitude passing through Indore is considered, which allows for a clear depiction of the evolution of instability and suppression across latitudes and time during the event. While CAPE provides information on the amount of energy available for the air parcels to undergo convection, CIN gives information about the resistance that prevents the parcels from rising to the level of free convection (LFC). Since CAPE and CIN are not directly provided by the IMDAA dataset, it has been estimated. Hovmöller diagrams of CAPE (row 1) and CIN (row 2) for Sets 1, 4, 8 and IMDAA are presented in Fig. 15. Although the values of CAPE from the model simulations are less intense than that from IMDAA, they follow the same pattern. Correspondingly, the magnitude of CIN from IMDAA is smaller than the three simulations. Set 1 can be seen to simulate stronger CAPE values over many of the regions prior to the rainfall than Set 8.

Simulations with and without KF CU in the innermost domain exhibited comparable CAPE values. Set 7 differs from Set 1 only in terms of the PBL scheme used. It can be seen that the CAPE values are weaker and the pattern is also different (Figures S30 and S31). As PBL schemes deal with the vertical mixing and the distribution of heat, moisture and momentum, they play an important role in the evolution of variables such as temperature and CAPE in the lower troposphere. Based on how the PBL schemes deal with the boundary layer mixing, each schemes treat CAPE differently. YSU being a non-local scheme, will tend to build the mixed layers more effectively, which may tend to deepen the convective environments more and lead to the underestimation of CAPE. MYJ on the other hand, is a local scheme and tends to trap moisture in the shallower boundary layers, it can lead to higher CAPE accumulation (Hong and Pan 1996). This could be the reason why among Sets 1 and 7, Set 1 performs better in capturing the CAPE.

Although Set 1 and Set 16 are just mirror simulations, with just the difference of CU scheme being used in the innermost domain, the CAPE values simulated follow similar patterns and Set 1 has a slightly stronger CAPE than Set 16. Theoretically, activating CU scheme in the domain of 2 km resolution could cause double-counting of convection, leading to lower CAPE than when CU is turned off. So, CAPE values simulated by Set 1 is supposed to be smaller than Set 16. However, Set 1 (910 J/kg) has a higher mean CAPE than Set 16 (882 J/kg). Although KF CU works on a CAPE based closure scheme by consuming CAPE within a particular timescale, it has a larger impact on the large-scale environment, which can ultimately affect the values of CAPE.Set 1 is found to have comparatively stronger vertical wind velocity than Set 16 as per the time-height variation plot in Figure S16. This difference can be distinctly seen between Sets 8 and 18 as well. The horizontal wind velocity simulated (Figure S17) are also found to be slightly stronger when KF is used as CU than when its turned off. The horizontal and vertical moisture flux is also higher for Sets 8 and 1 than 18 and 16, respectively (Figures S18, S19). The moisture present in the lower troposphere has an impact on the convection (Raymond 1995; Neelin et al. 2008). This, together with stronger vertical updrafts will create a more suitable environment for convection to take place and thereby contribute towards CAPE. In addition, since KF works on the basis of a trigger function, it allows the CAPE to develop sufficiently before its activation and consumption. This could be the reason of the high value of CAPE when KF was used as CU in d03.

The Sets 4, 7 and 8 only differs in the choice of MP schemes and the strength of the CAPE simulated by them varies. Set 4 simulates a comparably stronger CAPE, followed by Set 8 and then Set 7. However, on 16 September 2023, Set 7 is unable to capture CAPE values more than ≈ 1500 J/kg although all other Sets 1, 4 and 8 were able to do so. The impact of MP schemes can very well be seen in the dynamics associated (Figures S16, S19-S21). This indicates how the combination of PBL, CU and MP can significantly impact the simulation of convection.

It can be consistently observed from Fig. 13 and Fig. 15 that the simulations are underestimating the parameters when compared with IMDAA although the patterns are being captured. It is to be noted here that IMDAA is a reanalysis dataset and not a direct observational data. The differences observed could be attributed to the differences in the initial and lateral boundary conditions used in the two models. They also differ in terms of the physics and dynamics core used. The usage of data assimilation in reanalysis datasets is also a major difference, as this was not carried out for any of the simulations in this study. Comparing a model simulation with another model simulation comes with its own challenges as well. While the WRF simulations were made at a temporal resolution of 1 h with 44 eta-model vertical levels that extends up to 50 hPa, the pressure level variables from IMDAA are available at 3 hourly intervals with 18 pressure levels that extends upto 10 hPa. In addition, IMDAA was found to highly overestimate the rainfall during this period, which is in agreement with other studies as well (Akhter etal. 2025; Ghodichore et al. 2025). Various factors such as the stronger vertical velocity, moisture transport and extremely high CAPE values as observed could be the reason for the high overestimation of the rainfall parameter. Therefore, reanalysis datasets such as IMDAA cannot be considered as absolute truth. However, as domain-wide diagnosis cannot be carried out with observational data alone, this study has used IMDAA as a reference keeping in mind that there are limitations that arises with the usage of reanalysis data.

Discussions and conclusions

The Central India together with the northern region of BoB, also known as the Monsoon Core Zone, is one of the strongest convection regions in the Indian subcontinent. This is also one such region where MCS events are active. These systems contribute a significant amount of rainfall towards the Indian Summer Monsoon and plays a crucial role in the hydrological cycle. As an MCS passes through a region, it creates EREs and HREs along the way. Between 15-17 September 2023, the state of Madhya Pradesh had witnessed multiple EREs and HREs. Based on the IMD reports as well as the analysis of synoptic conditions from ERA5 dataset, this event is identified to be associated with an MCS event. 18 model simulations were carried out by varying MP, PBL and CU schemes at a "convection-permitting resolution" of 2 km to find the best performing model and to analyze how the models capture this event. Key observations made are listed below:

- All model simulations exhibited spatial and temporal delay in capturing the rainfall.
- All the simulations made with BMJ as CU had simulated significant rainfall and associated variables over the third day, which was not found in the observations, making it unsuitable for the study.
- Simulations with KF CU in the innermost domain exhibited better representation of rainfall and associated atmospheric conditions.
- Set 8 (Thompson MP + KF CU + YSU PBL) performed best among all the simulations followed by Set 4 (WSM6 MP + KF CU + YSU PBL) and Set 1 (Goddard MP + KF CU + MYJ PBL).
- The model analysis indicated that the system was primarily a low-to-mid level system that developed up to ≈17.5 km around the time of maximum rainfall, indicating the occurrence of deep convection at these times. This is in agreement with the analysis done from the reanalysis datasets.
- Although the best performing simulation was to capture the MCS event, the strength of the simulated system

dynamics was weaker than the IMDAA reanalysis, which may have led to the underestimation of the rainfall event.

The spatio-temporal delays and underestimation of EREs and HREs observed in this study is one of the challenges faced by the modelling community when the model is run at very high resolutions. The delay found in capturing the rainfall need not necessarily be due to the issues associated with the lead time. It could also be due to the initial conditions that are being used. While data assimilation can improve the spatio-temporal representation of rainfall, they can be computationally more expensive.

Although at convection-permitting resolutions, the models are expected to explicitly resolve the convection processes, in this study it was found that using KF CU in the innermost domain can help in capturing the rainfall associated with the MCS event better than when CU is turned off in this resolution. This also helps better represent the dynamics associated with the event and capture the MCS event that caused these rainfall events. While KF in this study proved to exhibit better performance, the convection-permitting resolution is a range where the traditional CU schemes are not typically recommended. However, in this case, simulations with CU turned off at 2 km were unable to capture the convection properly, which resulted in its high underestimation. This suggests that convection associated with MCSs may still benefit from CU parameterization under certain conditions. In such cases, the inclusion of a CU scheme may help trigger convection where explicit resolution is insufficient. In this context scale-aware version Multi-scale KF(MSKF) can also be explored as well to generalize these findings, more events need to be considered.

Overall, the study points to the combined influence of the CU, MP, and PBL schemes to capture the cause of the event. The temporal delay and underestimation of such EREs and HREs also indicate that there is a high requirement to improve the existing parameterization schemes.

Appendix A. Parameterization schemes used in the study

PBL schemes

Both types of closure schemes - local and non-local, have been considered in this study. MYJ, a local turbulence closure of order 1.5 based on the one-dimensional prognostic equation of turbulent kinetic energy (TKE) (Mellor and Yamada 1982) has been taken. This scheme calculates the vertical mixing and turbulence above the surface and accounts for momentum and mass transfer. YSU is another scheme that has been considered, a non-local turbulence closure of order one. It typically produces deeper and warmer daytime PBLs that often results in vertical mixing and entrainment (Hu et al. 2010; Arakawa 1975).

MP schemes

In this study, WSM6, Goddard and Thompson schemes are chosen as MP schemes. WSM6 is a single-moment bulk MP scheme that considers six hydrometeors: water vapor, cloud water, rain, cloud ice, snow and graupel (Hong and Lim 2006). Goddard is also a single-moment scheme similar to WSM6 and considers the same hydrometeors. However, it takes different assumptions to deal with the different hydrometeors (Tao and Simpson 1993). The Thompson scheme, on the other hand, is a double-moment scheme that considers the same set of hydrometeors but offers more detailed processes that help in mixed-phase dynamics (Thompson et al. 2008).

CU schemes

KF, BMJ and no CU options are considered for this study. Since the innermost domain of the model is run at a convection-permitting resolution, six simulations are made using KF as the CU for d01 and d02, with no cumulus in the innermost d03 domain as mentioned in Table 2. The KF is a mass-flux scheme that uses a simple cloud model to simulate the entrainment, detrainment and moist drafts. It calculates the strength of convection from the convective available potential energy (CAPE). This happens when an air parcel has a temperature greater than its surrounding parcels at its lifting condensation level and has a positive vertical velocity over a depth of at least 3-4 km (Kain and Fritsch 1990, 1993; Kain 2004). KF scheme gets triggered in the presence of deep convection. In addition, six simulations are designed with KF used as CU in the innermost domain. This is done to verify the model performance when CU is used within the convection-permitting resolution. Similarly, six simulations are designed using another CU scheme BMJ, which is a convection adjustment scheme. This scheme considers both shallow and deep convection to adjust the temperature and moisture profiles. The activation of this scheme is also similar to KF, i.e., it considers the convection strength based on the positive CAPE. In addition to this, it also requires the depth of the convective cloud to be beyond a particular threshold and also the moist soundings in order to activate (Janjić 1994; Betts and Miller 1984).

Radiation scheme-longwave and shortwave

These schemes deal with the radiative fluxes in the atmosphere and parameterize them in the model. Dudhia shortwave radiation scheme, one of the most commonly used schemes, is used in this study (Madhulatha and Rajeevan 2018; Gunwani et al. 2021; Musaid et al. 2023). This scheme uses a simple downward integration for absorption and scattering (Dudhia 1989). To parameterize the longwave radiation, the rapid radiative transfer model for general circulation (RRTMG) is used. This is a version of RRTM that makes use of the Monte Carlo Independent Column Approximation (McICA). This scheme considers a random overlapping of the clouds instead of uniform overlap (Mlawer et al. 1997; Iacono 2011).

LSM scheme

LSM schemes represent the land-atmospheric interactions. These in turn have an impact on the precipitation forecasts as they affect the near-surface temperature and humidity. They play a crucial role in the simulation of heat and moisture fluxes. Unified Noah LSM scheme is used in this study to account for these interactions (Chen and Dudhia 2001). This scheme considers the surface-energy balance, evapotranspiration, soil moisture and other variables. It also incorporates four soil layers, vegetation and key hydrological processes.

Appendix B. Equations for various statistical metrics used

$$RMSE = \sqrt{\frac{\sum_{i=1}^{N}(y_i - o_i)^2}{N}} \tag{A1}$$

$$MAE = \frac{\sum_{i=1}^{N}|y_i - o_i|}{N} \tag{A2}$$

$$MB = \frac{\sum_{i=1}^{N} y_i - o_i}{N} \tag{A3}$$

$$CC = \frac{\sum_{i=1}^{N}(y_i - \bar{y})(o_i - \bar{o})}{\sqrt{\sum_{i=1}^{N}(y_i - \bar{y})^2}\sqrt{\sum_{i=1}^{N}(o_i - \bar{o})^2}} \tag{A4}$$

$$POD = \frac{a}{a + c} \tag{A5}$$

$$FAR = \frac{b}{a + b} \tag{A6}$$

$$CSI = \frac{a}{a + b + c} \tag{A7}$$

$$ETS = \frac{a - a_r}{a - a_r + b + c}\, where\, a_r = \frac{(a + b)(a + c)}{a + b + c + d} \tag{A8}$$

where, N is the total number of data points, y_i is the i^{th} data or model output value and o_i is its corresponding observation value. $\bar{y}$ and $\bar{o}$ corresponds to the mean of data or model and observation. a, b and c represents the marginals as shown in Fig. 3.

Supplementary Information The online version contains supplementary material available at https://doi.org/10.1007/s40808-025-02715-2.

Acknowledgements The authors are greatful to IMD, NCMRWF, ISRO, ECMWF, NCAR, NASA and JAXA for the open source datasets that have been used in this study.

Author contributions P.T. took part in methodology, carried out the data curation and model simulation, conducted formal analysis and investigation, and prepared the original draft. S.D. conceptualized the study, took part in methodology, supervision, and contributed in reviewing and editing the manuscript.

Funding The study was supported by MoES NARM program (MoES/16/04/2021-RDESS/NARM-4) and the SERB (CRG/2022/006986).

Data availability No datasets were generated or analysed during the current study.

Declarations

Conflict of interest The authors declare no competing interests.

References

Aggarwal D, Attada R, Shukla K et al (2022) Monsoon precipitation characteristics and extreme precipitation events over northwest India using Indian high resolution regional reanalysis. Atmos Res 267:105993

Akhter J, Sarkar S, Choudhury RR et al (2025) Performance analysis of imdaa and era5 reanalysis in reproducing monsoon precipitation extremes over eastern India: J. akhter et al. Theoret Appl Climatol 156(7):371

Ali H, Mishra V (2017) Contrasting response of rainfall extremes to increase in surface air and dewpoint temperatures at urban locations in India. Sci Rep 7(1):1228

Arakawa A (1975) Modelling clouds and cloud processes for use in climate models. WMO The Phys Basis of Climate and Climate Modelling p 183-197(SEE N 76-19675 10-47)

Ashok R, Singh KS (2025) Role of microphysical processes in a convection permitting scale for the simulation of Arabian Sea tropical cyclones using wrf model. Model Earth Syst Environ 11(3):172

Betts AK, Miller M (1984) A new convective adjustment scheme. 43, European Centre for Medium Range Weather Forecasts

Bjerge B, Trifkovic N (2018) Extreme weather and demand for index insurance in rural India. Eur Rev Agric Econ 45(3):397–431

Boyaj A, Dasari HP, Hoteit I et al (2020) Increasing heavy rainfall events in South India due to changing land use and land cover. Q J R Meteorol Soc 146(732):3064–3085

Chawla I, Osuri KK, Mujumdar PP et al (2018) Assessment of the weather research and forecasting (wrf) model for simulation of extreme rainfall events in the upper ganga basin. Hydrol Earth Syst Sci 22(2):1095–1117

Chen F, Dudhia J (2001) Coupling an advanced land surface-hydrology model with the penn state-ncar mm5 modeling system. part i: Model implementation and sensitivity. Mon Weather Rev 129(4):569–585

Deng A, Stauffer DR (2006) On improving 4-km mesoscale model simulations. J Appl Meteorol Climatol 45(3):361–381

Douluri DL, Chakraborty A (2021) Assessment of wrf-arw model parameterization schemes for extreme heavy precipitation events associated with atmospheric rivers over west coast of India. Atmos Res 249:105330

Dudhia J (1989) Numerical study of convection observed during the winter monsoon experiment using a mesoscale two-dimensional model. J Atmos Sci 46(20):3077–3107

Eiras-Barca J, Dominguez F, Hu H et al (2017) Evaluation of the moisture sources in two extreme landfalling atmospheric river events using an Eulerian wrf tracers tool. Earth Syst Dyn 8(4):1247–1261

Evans JP, Ekström M, Ji F (2012) Evaluating the performance of a wrf physics ensemble over south-east Australia. Clim Dyn 39:1241–1258

Garratt JR (1994) The atmospheric boundary layer. Earth Sci Rev 37(1–2):89–134

Ghodichore N, Sinha MK, Sahu A (2025) Assessing the performance of reanalysis climatic data in reproducing past precipitation and temperature patterns in India. J Water Clim Chang 16(3):1136–1161

Gimhan P, Neluwala P, Acierto RA (2023) High-resolution wrf simulations of a monsoon event (2019) over the Badulu Oya catchment, Sri Lanka: role of cumulus parameterization condition and microphysics schemes. J Earth Syst Sci 132(4):166

Gorja MMK, Challa VS, Viswanadhapalli Y et al (2023) Sensitivity of cloud microphysics on the simulation of heavy rainfall in wrf-a case study for the 7–10 august 2019 event over kerala, India. Atmos Res 288:106715

Goswami BN, Venugopal V, Sengupta D et al (2006) Increasing trend of extreme rain events over India in a warming environment. Sci 314(5804):1442–1445

Gunwani P, Mohan M (2017) Sensitivity of wrf model estimates to various pbl parameterizations in different climatic zones over India. Atmos Res 194:43–65

Gunwani P, Sati AP, Mohan M et al (2021) Assessment of physical parameterization schemes in wrf over national capital region of India. Meteorol Atmos Phys 133:399–418

Gupta P, Verma S, Mukhopadhyay P et al (2024) Fidelity of wrf model in simulating heat wave events over India. Sci Rep 14(1):2693

Hatheway W, Snoun H, ur Rehman H et al (2023) Wrf-mosit: a modular and cross-platform tool for configuring and installing the wrf model. Earth Sci Inf 16(4):4327–4336

Hong SY, Lim JOJ (2006) The wrf single-moment 6-class microphysics scheme (wsm6). Asia-Pac J Atmos Sci 42(2):129–151

Hong SY, Pan HL (1996) Nonlocal boundary layer vertical diffusion in a medium-range forecast model. Mon Weather Rev 124(10):2322

Hu XM, Nielsen-Gammon JW, Zhang F (2010) Evaluation of three planetary boundary layer schemes in the wrf model. J Appl Meteorol Climatol 49(9):1831–1844

Huffman GJ, Bolvin DT, Braithwaite D et al (2015) Nasa global precipitation measurement (gpm) integrated multi-satellite retrievals for gpm (imerg). Algorithm theoretical basis document (ATBD) version 4(26):2020–05

Iacono MJ (2011) Application of improved radiation modeling to general circulation models. Tech. rep, Atmospheric and Environmental Research Inc, Lexington, MA (United States)

IMD (2023a) Annual report 2023. https://drive.google.com/file/d/1lMww9NGffovRLODAPa_UWBOT4xW5HNZ-/view, Accessed 26 Apr 2025

IMD (2023b) Press release dated 11 september 2023. https://internal.imd.gov.in/press_release/20230911_pr_2523.pdf, Accessed 26 Apr 2025

IMD (2023c) Press release dated 12 september 2023. https://internal.imd.gov.in/press_release/20230912_pr_2524.pdf, Accessed 26 Apr 2025

IMD (2023d) Press release dated 13 september 2023. https://internal.imd.gov.in/press_release/20230913_pr_2525.pdf, Accessed 26 Apr 2025

IMD (2023e) Press release dated 14 september 2023. https://internal.imd.gov.in/press_release/20230914_pr_2527.pdf, Accessed 26 Apr 2025

IMD (2023f) Press release dated 16 september 2023. https://internal.imd.gov.in/press_release/20230916_pr_2529.pdf, Accessed 26 Apr 2025

IMD (2023g) Press release dated 17 september 2023. https://internal.imd.gov.in/press_release/20230917_pr_2530.pdf, Accessed 26 Apr 2025

Janjić ZI (1994) The step-mountain eta coordinate model: further developments of the convection, viscous sublayer, and turbulence closure schemes. Mon Weather Rev 122(5):927–945

Jankov I, Gallus WA, Segal M et al (2005) The impact of different wrf model physical parameterizations and their interactions on warm season mcs rainfall. Weather Forecast 20(6):1048–1060

Jee JB, Kim S (2017) Sensitivity study on high-resolution wrf precipitation forecast for a heavy rainfall event. Atmosphere 8(6):96

Kadaverugu R, Matli C, Biniwale R (2021) Suitability of wrf model for simulating meteorological variables in rural, semi-urban and urban environments of central India. Meteorol Atmos Phys 133(4):1379–1393

Kain JS (2004) The Kain-Fritsch convective parameterization: an update. J Appl Meteorol 43(1):170–181

Kain JS, Fritsch JM (1990) A one-dimensional entraining/detraining plume model and its application in convective parameterization. J Atmos Sci 47(23):2784–2802

Kain JS, Fritsch JM (1993) Convective parameterization for mesoscale models: The Kain-Fritsch scheme. In: The representation of cumulus convection in numerical models. Springer, p 165–170

Karrevula NR, Nadimpalli R, Sinha P et al (2024) Performance evaluation of wrf model in simulating extreme rainfall events over Bhubaneswar urban region of east coast of India. Pure Appl Geophys 181(12):3605–3631

Lee SW, Lee DK, Chang DE (2011) Impact of horizontal resolution and cumulus parameterization scheme on the simulation of heavy rainfall events over the korean peninsula. Adv Atmos Sci 28:1–15

Liang XZ, Li Q, Mei H et al (2019) Multi-grid nesting ability to represent convections across the gray zone. J Adv Model Earth Syst 11(12):4352–4376

Madhulatha A, Rajeevan M (2018) Impact of different parameterization schemes on simulation of mesoscale convective system over south-east India. Meteorol Atmos Phys 130:49–65

Mellor GL, Yamada T (1982) Development of a turbulence closure model for geophysical fluid problems. Rev Geophys 20(4):851–875

Milrad SM, Lombardo K, Atallah EH et al (2017) Numerical simulations of the 2013 Alberta flood: dynamics, thermodynamics, and the role of orography. Mon Weather Rev 145(8):3049–3072

Mlawer EJ, Taubman SJ, Brown PD et al (1997) Radiative transfer for inhomogeneous atmospheres: Rrtm, a validated correlated-k model for the longwave. J Geophys Res Atmos 102(D14):16663–16682

Mohapatra M, Sharma M (2019) Cyclone warning services in India during recent years: a review. Mausam 70(4):635–666

Mondal U, Kumar A, Panda SK et al (2024) Comprehensive study of thunderstorm indices threshold favorable for thunderstorms during monsoon season using wrf-arw model and era5 over India. Geoenviron Disasters 11(1):13

Mukherjee P, Ramakrishnan B (2022) On the understanding of very severe cyclone storm Ockhi with the wrf-arw model. Environ Res Clim 1(1):015002

Musaid P, Manoj M, Panda SK et al (2023) Dynamical influence of west pacific typhoons on the 2018 historic flood of kerala as revealed by the weather research and forecasting (wrf) model. Clim Dyn 61(3):1663–1681

Neelin JD, Peters O, Lin JWB et al (2008) Rethinking convective quasi-equilibrium: observational constraints for stochastic convective schemes in climate models. Philos Trans R Soc A Math Phys Eng Sci 366(1875):2579–2602

Pai D, Sridhar L (2015) Long term trends in the extreme rainfall events over India. High-impact weather events over the SAARC region pp 229–240

Park H, Kim G, Cha DH et al (2022) Effect of a scale-aware convective parameterization scheme on the simulation of convective cells-related heavy rainfall in south korea. J Adv Model Earth Syst 14(6):e2021MS002696

Patil R, Pradeep Kumar P (2016) Wrf model sensitivity for simulating intense western disturbances over north west India. Model Earth Syst Environ 2:1–15

Pérez-Alarcón A, Vázquez M, Trigo RM et al (2024) Evaluation of wrf model configurations for dynamic downscaling of tropical cyclones activity over the north Atlantic basin for lagrangian moisture tracking analysis in future climate. Atmos Res 307:107498

Rani SI, Arulalan T, George JP et al (2021) Imdaa: High-resolution satellite-era reanalysis for the Indian monsoon region. J Clim 34(12):5109–5133

Raymond DJ (1995) Regulation of moist convection over the west pacific warm pool. J Atmos Sci 52(22):3945–3959

Roberts NM, Lean HW (2008) Scale-selective verification of rainfall accumulations from high-resolution forecasts of convective events. Mon Weather Rev 136(1):78–97

Rohini P, Rajeevan M, Srivastava A (2016) On the variability and increasing trends of heat waves over India. Sci Rep 6(1):1–9

Seo GY, Ahn JB (2023) Comparative study on the characteristics of rainfall simulation over South Korea by summertime weather patterns according to the use of cumulus parameterization. Theoret Appl Climatol 154(3):907–924

Shaji A, Manoj M, Johny K et al (2024) Investigation of moist thermodynamical processes of a tropical thunderstorm using 205 mhz vhf radar and wrf model. Model Earth Syst Environ 10(3):4497–4511

Sharma A, Sharma D, Panda S et al (2024) Sensitivity analysis of different parameterization schemes of the weather research and forecasting (wrf) model to simulate heavy rainfall events over the mahi river basin, India. Agric For Meteorol 346:109885

Singh V, Goyal MK (2016) Changes in climate extremes by the use of cmip5 coupled climate models over eastern Himalayas. Environ Earth Sci 75:1–27

Skamarock W, Klemp J, Dudhia J, et al (2021) A description of the advanced research wrf model version 4.3; no. NCAR/TN556+STR

Srinivas C, Hariprasad D, Bhaskar Rao D et al (2013) Simulation of the Indian summer monsoon regional climate using advanced research wrf model. Int J Climatol 33(5):1195–1210

Tao WK, Simpson J (1993) The Goddard cumulus ensemble model. part i: Model description. Terr Atmos Oceanic Sci 4(1):35–72

Thompson G, Field PR, Rasmussen RM et al (2008) Explicit forecasts of winter precipitation using an improved bulk microphysics scheme. part ii: Implementation of a new snow parameterization. Mon Weather Rev 136(12):5095–5115

Tiwari U, Bush AB (2025) Significance of cloud microphysics and cumulus parameterization schemes in simulating an extreme flood-producing precipitation event in the central himalaya. Atmosphere 16(3):298

Ueida L, Tian D, Leong WJ, et al (2021) Pygmt: a python interface for the generic mapping tools. https://doi.org/10.5281/ZENODO.4522136. Accessed 17 July 2025

Wang T, Zhu J, Lei H et al (2022) Comparison of microphysics parameterization schemes on cloud macrophysics forecasts for mixed convective-stratiform cloud events. Atmos Res 277:106284

Zhou P, Ma M, Shao M et al (2024) Sensitivity of summer precipitation simulation to the physical parameterizations in wrf over the Tibetan plateau: a case study of 2018. Atmos Res 299:107174